LSU Doctoral Dissertations   Graduate School

2014

Continuous reservoir modeling updating by integrating experimental data using an ensemble Kalman Filter

Ting Sun
Louisiana State University and Agricultural and Mechanical College, tsun2@tigers.lsu.edu

CONTINUOUS RESERVOIR MODELING UPDATING
BY INTEGRATING EXPERIMENTAL DATA
USING AN ENSEMBLE KALMAN FILTER

A Dissertation

Submitted to the Graduate Faculty of the
Louisiana State University and
Agricultural and Mechanical College
in partial fulfillment of the
requirements for the degree of
Doctor of Philosophy

in

The Craft & Hawkins Department of Petroleum Engineering

by
Ting Sun
B.S., China University of Petroleum, 2005
M.S., China University of Petroleum, 2008
May 2014

This dissertation is dedicated to my parents, for their unconditional love, to my wife, for the encouragement she gave, to my son, who changes the entire of my world.

Acknowledgments

The dissertation would not be possible without several contributions. I would like to express the deepest appreciation to my previous advisor, Dr. Christopher D. White, for his valuable guidance, encouragement and support. Without his supervision and persistent help this dissertation would not have been possible.

I want to thank my advisor, Dr. Arash Dahi, for his help on my research work, especially the suggestion of re-doing the sand tank experiment which made my dissertation more convincing. Thanks for his patience and dedication of his time.

I would also thank my co-advisor, Dr. Juan Lorenzo, for his help on sand tank experiment and the valuable suggestions both on research work and dissertation writings. I cannot finish my dissertation without his help.

I would also like to extend my appreciations to Dr. Mayank Tyagi for his guidance throughout my graduate study and Dr. Karsten Thompson for being my committee and helping me graduate.

Finally, I extend many thanks to all my colleagues and friends in LSU for their company and help especially thanks Yuanyuan Shuai, Yin Feng, Jie Shen and Shannon Chollett, for their valuable discussions and help on my research.

Contents

Abstract

The continuous researvoir model updating is widely used to calibrate reservoir simulation models to production data, but many challenges remain. First, few real field data are available to test the new history matching method, and most of the data sets are synthetic cases. Second, computational cost may be high when using non-Gaussian priors or nonlinear models. Third, with large complex models, the simulation runs and history matching method require huge memory allocations.

This dissertation achieves a continuous reservoir model updating workflow with a meter–scale , two–phase flow experiment. Both production and seismic data are collected in the experiment. Because the data are high–frequency sequential data with noise, the EnKF method is used to efficiently integrate them.

To better understand the problem, scaling analysis is done on the capillary transition zone. Two new dimensionless numbers are introduced—capillary time and capillary length. We found that for different models, if their capillary time and gravity number are equal, the capillary length would be the same. The scaling analysis results help us find a proper flow rate for the sand tank experiment.

Two experiments are conducted to test the workflow and the EnKF method. In the first one, both the production and seismic data are collected and analyzed. The production data have large errors in the flow rate and they are integrated to improve reservoir models using EnKF method. The history matching results are in an acceptable range which demonstrate that even if the observation data has large error, the EnKF method still works. In the second experiment, the errors of flow rate are reduced by measuring manually with a graduated cylinder. Because the data quality are much better in the second experiment, the observations can be matched easily.

Chapter 1
Introduction

1.1 Background

Reservoir history matching is the calibration of a reservoir model to dynamic data using numerical simulators. It has been one of the longstanding challenges of forecasting (Alpak et al., 2009).

Reservoir modeling is one of the key components needed to: 1) understand the geologic and reservoir model; and 2) forecast reservoir behavior with a known degree of confidence. Traditionally, history matching is done by varying a few reservoir parameters manually until a satisfactory match is achieved. It is time–consuming and only lead to a single, so called, "best" history-matched model (Tavassoli et al, 2004). Because reservoir models have a large number of model parameters (e.g., 10^6) and fewer observed data (e.g., 10^2), history matching problems are underconstrained and their results are nonunique. One "best" model cannot capture the uncertainties of reservoir forecasts.

A Bayesian framework has been considered in reservoir history matching (Tarantola, 1997), and constitutes a statistically consistent way of updating a set of models subject to observed data. In recent years, the development of automatic history matching methods and increased computational capacity allows us to achieve more than one "best" model to analyze the uncertainty. Reservoir engineers reduce the uncertainty of reservoir models by integrating different types of data when they are available. For example, production data, core analysis results and seismic data can all be included. Reservoir development teams can then optmize the reservoir development strategy in the presence of uncertainty. Sometimes we simply aim to

assess the uncertainty, even when there are not new or abundant data to reduce uncertainty. Assessment is valuable, even if it is rarely done.

1.2 Problem Statement

The performance of oil and gas reservoirs must be predicted to plan their development profitably and efficiently. However, prediction is difficult because fluid and especially rock properties are uncertain, and the equations used to describe flows in reservoirs are nonlinear (Oliver, 2008). In this dissertation, these problems are addressed by using a commercial reservoir simulator to solve the flow equations and by using an ensemble inversion method to integrate the observation data and estimate uncertain properties. Systematic statement of observation errors and a priori probability of models allows statistically and physically correct propagation of uncertainty, and provides estimates of uncertainties in both properties and predictions.

Automatic history matching methods have been well developed, and the Ensemble Kalman Filter (EnKF) method and its variants are among the most promising contemporary methods (Watanabe et al., 2009; Schulze-Riegert et al., 2009; Li et al., 2008). The main challenges when using the EnKF to update reservoir simulation models are related to the low rank representation of the model covariance matrix, non-Gaussian prior models, strong nonlinearities in the forward model and the application to large scale field models (Aaninsen, 2008). Solving these challenges increases the computational cost, especially in strongly nonlinear models. Meanwhile, as reservoir models becoming consistently larger over time, computational cost must be considered when using an EnKF method. Computational cost can be reduced by solving the strong nonlinearities more efficiently, or by parallelizing the reservoir simulation runs and the calculations of Kalman gain (Li, 2008).

Another challenge is the data integration to calibrate the models. Commonly the history matching results are poor when only production data are integrated. Because there are too few wells, and the wells are typically clustered in high–quality or updip areas, which leaves the other regions unconstrained (Dong, 2005). Seismic data can be integrated with production data to improve the estimation. Dong (2005) proposed an approach to integrate seismic data, but the seismic data first has to be inverted to seismic impedance values, which are also nonunique (Saltzer and Finn, 2006). Integrating seismic data without a separate inversion step is a promising approach.

1.3 Current Approaches
1.3.1 Traditional History Matching Algorithms

History matching algorithms can be classified into two main categories, gradient–free and gradient–based. Gradient–free methods require no modification of the simulation software, and can be formulated to avoid local optima. Some well known examples of gradient–free methods include simulated annealing (Ouenes et al., 1993; Deutsch and Journel, 1994), genetic algorithms (Sen et al., 1995) and neighborhood algorithm (Sambridge, 1999). Although nongradient methods can be used to find the global minimization point, they may require millions of simulations to converge. When model size becomes large, the computational cost tends to be prohibitive.

Among gradient–based methods, the Gauss-Newton and the Levenberg-Marquardt methods (Li et al., 2003) are widely used because of their quadratic convergence rate. However, it becomes impractically expensive to store the matrix when the model size is large, or to compute sensitivity coefficients and the Hessian matrix (second derivative) of the objective function when the number of data is large. In contrast, Newton type methods, which are also gradient–based, require only the

gradient of the objective function because the Hessian is approximated by a product of the components of the gradient. Gradient–based methods include steepest descent, conjugate gradient and the Limited Memory Broyden-Fletcher-Goldfarb-Shanno (LBFGS) method (Chen, 2008). In gradient based methods, an efficient method to compute the gradient of the objective function is the adjoint method (Zhang and Reynolds, 2002; Zhang et al., 2005).

Although automatic history matching can integrate observation data using the adjoint method and LBFGS method, these methods have drawbacks. First, the adjoint equations require modifying the source code of the reservoir simulator; this is difficult to do with commercial simulators. Secondly, the adjoint method and LBFGS method are good at finding local minima, but commonly fail to find the global optimum. Thirdly, the observed data become dense in the time domain and it is impractical to incorporate all the data simultaneously. Finally, for uncertainty analysis, it is necessary to have a set of history-matched models. Considering the time used to achieve one minimization, it may not be feasible to obtain an ensemble of estimated reservoir simulation models to analyze uncertainty (Zhang and Reynolds, 2002; Gao and Reynolds, 2006). Therefore, an investigation of alternative automatic history matching methods is worthwhile. For large scale nonlinear systems, the Ensemble Kalman Filter is promising.

1.3.2   Ensemble Kalman Filter

The Ensemble Kalman Filter is a Bayesian approach; the EnKF is initialized by generating an ensemble of plausible reservoir models using a priori geostatistical assumptions (Wen and Chen, 2007). Initialization commonly uses a conditional simulation (Goovaerts, 1997), although more sophisticated approaches such as multipoint geostatistics (Strebelle, 2002) or stratal modeling (Pyrcz, 2004; Kalla et al., 2008) may be used. The EnKF continuously updates the ensemble of reser-

voir models whenever new observations are available. The EnKF yields a group of history–matched models, which are suitable for uncertainty analysis. The EnKF method does not require adjoint equations and is loosely coupled to the forward model (the reservoir simulator). The updated variables are static fields, dynamic fields, and additional parameters (such as permeability multipliers and fault transmissibility multipliers). That is, the dependent variables (such as saturation and pressure) are updated along with the history match parameters (such as permeability). This raises questions about model consistency, which have been addressed in the literature (Wen and Chen, 2007) and will be discussed in this dissertation.

The EnKF was introduced by Evensen (1994) as a modification of the Kalman filter for nonlinear problems. The EnKF has been applied in oceanography (Echevin et al., 2000) and meteorology (Madsen and Canizares,1999). The EnKF was introduced to reservoir history matching by Lorentzen et al. (2001). Nævdal et al. (2002) applied the EnKF to estimate the permeability on a 2D field–like synthetic example.

Because the EnKF assumes Gaussian priors and linear model dynamics, the EnKF may not work properly when the posterior distribution is non-Gaussian or the relationships between model parameters, state variables, and observations are strongly nonlinear. Variants of EnKF have been developed to address these problems. Anderson (2001), Houtekamer and Mitchell (2001) and Evensen (2004) presented the square root algorithm which updates the ensemble perturbations; they also derived a new covariance update. Gu and Oliver (2005) showed that it is possible to generate nonphysical values during the update steps of the EnKF; they suggested a change of variables or iteration. Reynolds et al. (2006) present an Iterative EnKF (IEnKF) method to solve the nonlinear and non-Gaussian prob-

lems. Wen and Chen (2007) introduced a confirming option in EnKF to keep the updated static and dynamic variables consistent.

Li (2008) compared the EnKF with reparameterization and the EnKF with truncation, and concluded that they have similar estimation results; EnKF with truncation requires less computational time and storage space. Chen et al. (2009) applied an EnKF with reparameterization to address the non-Gaussian effect and obtained a realistic water saturation distribution.

In the past two years, hybrid methods have become popular in the application of EnKF method. Hybrid methods couple EnKF methods and another method to address the nonlinear and non-Gaussian effects (Watanabe et al., 2009; Schulze-Riegert et al., 2009; Li et al., 2008), but hybrid methods require more computation.

Because the problem addressed in this dissertation is not strongly nonlinear or non-Gaussian, the standard EnKF will be used as the history matching method in this dissertation and the formulas will be introduced in Chapter six.

1.3.3 Integrated Data

Improved modeling has helped to optimize reservoir development. To reduce the inherent uncertainty of the models and obtain more predictive simulations, more data should be integrated into the geomodels. Production data, such as bottom hole pressure, gas oil ratio and water oil ratio have been widely used in history matching. Interwell tracer tests, well testing and seismic data also provide additional sources of data. Thulin et al. (2007) show that when production data are integrated into reservoir models with the standard EnKF method, it is relatively easy to account for uncertainty in the depths of the initial fluid contacts and provide estimates of these depths in addition to the traditional estimates of rock properties fields. Li et al. (2009) applied the EnKF method to the integration of well test data into heterogeneous reservoir models. They concluded that better data matches

are obtained after integrating pressure transient data. Valestrand et al. (2010) coupled the EnKF methodology with chemical tracer data. The permeability and the fault transmissibility multiplier in a 2D test example are successfully estimated by including tracer data in the EnKF estimation. Moreover, they show that the tracer data improve inversion overestimations.

Although production data, well testing data and tracer data can provide high resolution estimation around well locations, properties in regions far from wells remain poorly constrained. To reduce uncertainty in estimation, seismic data can be integrated with production data to provide denser information across whole field. Many investigators have addressed seismic data integration and proved that seismic data can help improve the reservoir models. Gosselin et al. (2003) have presented the development of software that includes production and inverted seismic data in the history matching process. They used a case to show the improvement of matched models by integrating 4D seismic data. Dong (2005) integrated seismic impedance changes with the production data using the adjoint method and LBFGS method. The results showed that the integration of seismic impedance changes can improve predictions. Emerick et al. (2007) integrated time–lapse seismic attributes into a derivative-based assisted history matching tool; their optimization algorithm was based on a trust-region quasi-Newton method to minimize the mismatch between observed and simulated data from production and seismic. Dong (2005) applied the EnKF method to rapidly update the estimation of the model variables in a small synthetic case which shows that it is possible to integrate both time–lapse seismic impedance data and production data using the EnKF. A method based on the combination of EnKF and EnKS (Skjervheim et al., 2007) used a combination of production data and 4D seismic data. Their method was tested on a synthetic case and a real North Sea field case. For both the synthetic and field

case, a better permeability estimate was obtained by including both seismic data and production data. For the 2D synthetic problem, better estimates of the permeability were obtained by integrating inverted seismic data at the time they were measured instead of using 4D data. Zhao et al. (2008) proposed integrating seismic data (acoustic impedance data) at two separate times together with production data. They gave an ensemble of facies maps closer to the "true model" and better estimates of future performance than the ones obtained from the models updated by production data only.

In conclusion, seismic data can be integrated to improve the reservoir models. However, the integration of seismic data still has several drawbacks. First, for time–lapse seismic data integration, some reservoirs may not express enough changes in seismic properties. Second, the time–lapse method generally assumes that the source and receiver do not change over time. Third, seismic inversion is nonunique (Gunning and Glinsky, 2004). For example, using the same seismic data, many different seismic impedance datasets can be obtained, all of which are plausible. Finally, seismic data are indirect sources of formation velocities. The velocities of the formation depend on the density and elastic moduli of the rock–fluid system, both of which are influenced by water saturation, especially when the water saturation approaches one. Understanding the saturation distribution is very important in determining the velocity model.

1.3.4   Sand Tank Experiment

Modeling is used to obtain a better understanding of problems. There are two categories of modeling – physical modeling and numerical modeling. Physical modeling is based on actual observations whereas numerical modeling uses partial differential equations that are simplified and discretized expressions of the real world. Although numerical modeling has been used widely, physical modeling is still needed

to validate mathematical models (Vinsome and Westerveld, 1980) and study the physical world (Ahner and Sufi, 1994). It should be emphasized that the validated model can address the right problem and provide accurate information about the system being modeled, but it does not mean that the validated models represent the actual processes in the real-world system accurately (Oreskes et al., 1994).

The problem addressed in this dissertation is air displacing water (or vice versa) in a meter–scale physical flow model. This physical model, the "sand tank", is equipped with accelerometers for seismic refraction surveys, pressure and temperature sensors, and a flow meter for water production rate. Also some saturation sensors will be placed in future to validate history matching results or provide more observation data for integration. This diverse data set poses challenges for data integration, but will provide a meaningful, repeatable experiment to examine algorithm performance and assess the value of data. This air–water system is an analog of gas–oil displacements in an exploration and production setting (Smolkin, 2011). Chapter two will introduce the sand tank experiment and the calculation of flow and seismic properties.

The sand tank experiment provides production rate, bottom hole pressure and seismic first arrival data which will be integrated using the EnKF method. The production data will be integrated in the traditional way. For the first arrival time of seismic data, both the synthetic, computed first arrival time and the observed first arrival times are needed. The seismic raytracing result is obtained using FAST (Zelt, 1988), a 2-D seismic tomography program. The velocity models are computed from reservoir simulation results by the Hertz–Mindlin method (Bachrach et al., 1998b). The observed first arrival time is picked from the seismic data of the experiment by a first arrival auto-picking program in Seismic Unix (Center for Wave Phenomena, 2012). For the water and air system, the velocity is impacted

by the capillary transition zone, thus the inspectional analysis is used to summarize the transition behavior.

1.3.5 Scaling Analysis of Transition Zones

In an air-water system, saturation varies in the transition zone, which is controlled by capillary pressures and flow rates. In Chapter three, scaling analysis help us have a better understanding of the behavior of the capillary transition zone and predict the saturation distribution.

Scaling analysis characterizes similar behavior at different length and time scales, and for different system properties or states(e.g., velocity and viscosity). Scaling analysis reduces the number of parameters of a model to several dimensionless numbers. For two reservoirs, when their dimensionless numbers are equal, their dimensionless-dependent variables will be the same. Based on scaling analysis, we can translate the results obtained from one scale to another, usually from a small–scale laboratory observation to a large–scale process.

There are two ways to obtain dimensionless groups used in scaling: dimensional analysis (Buckingham, 1914) and inspectional analysis (Ruark, 1935). Dimensional analysis is the analysis of the relationships between different physical parameters, and the dimension of any physical parameters can be expressed by a combination of basic physical dimensions which can be used for scaling analysis without honoring the governing equation. Inspectional analysis is an extension of dimensional analysis since it considers the governing equations. Inspectional analysis is based on the underlying mathematical–physical laws expressed by partial differential equations and boundary conditions. Inspectional analysis is preferred in petroleum related literature, such as the work by Shook et al. (1992).

The capillary transition zone in the **water-air** system is located between the water-air contact and the level where irreducible water is present. The water-air

contact occurs at a single elevation, z_{aw}, typically chosen such that $P_c\left(S(z_{aw})\right) = 0$, where P_c is capillary pressure, $S(z_{aw})$ is the saturation at z_{aw} (Ahmed, 2010). The transition zone is an interval, $S_w(z) \in (S_{wi}, 1 - S_{ar})$, where S_{wi} is irreducible water saturation and S_{ar} is residual air saturation. The transition zone is very important for modeling, and is usually named as "capillary transition zone" – it is also defined as the mixing zone that occurs between two phases due to the capillary pressure generated when the fluids are immiscible.

If the dimensionless groups and independent variables are matched at different scales, dimensionless dependent variables such as the recovery efficiencies will have equal values to each other. Shook et al. (1992) investigated how the breakthrough recovery efficiency changes with the buoyancy number and gravity number, but the dimensionless mixing zone behavior in time was not discussed.

Eigestad and Larsen (2000) incorporate hysteresis for a capillary pressure and relative permeability in a simulator and present test cases with vertical fluid flow in a homogeneous reservoir at different injection and production rates. Although they have shown how the transition zone changes with different production or injection rates, there was no quantitive analysis.

1.3.6 Seismic Resolvability of Transition Zones

Seismology is the study of earthquakes and earth structures through both natural and artificially generated seismic waves, which penetrate through formations and return to the surface as reflections and refractions. The seismic signals received on the surface help estimate the properties of the formation, such as the density of rock and fluid, saturation, porosity and effective pressure.

Water saturation varies with depth in the capillary transition zone, and influences both seismic reflections and refractions. Based on the Hertz–Mindlin model, wave velocities increase sharply when water saturation approaches one. This phe-

nomenon can be used to locate the lower boundary of capillary transition zones. Bachrach et al. (1998b) concluded that for monitoring water table changes during pumping, the seismic response is controlled by both the saturation profile and the water table.

Chapter four will focus on using first arrival time of seismic data to locate the capillary transition zone. The seismic first arrival is the first signal detected by the geophone. Its path depends on the spatial variation of acoustic velocity in the vicinity of the source and geophone. Generally, acoustic rays are refracted across interfaces where velocity changes. Because the earliest portion of the seismic record is often dominated by source generated noise, first–arrival data are more accurate and can be more clearly identified than reflected wave data. The first arrival of seismic data has been used for mapping depth of landfills, the thickness of the overburden and the topography of ground water (Yilmaz, 2001).

1.4   Objectives and Research Scope

The main objectives of this dissertation are to 1) apply the Ensemble Kalman Filter (EnKF) to the sand tank experiment data integration and 2) demonstrate the feasibility of integrating the seismic first arrivals into reservoir models. To better understand the problem, sand tank transport and acoustic properties are calculated, and scaling analysis and seismic resolvability have been done for the capillary transition zone.

There are eight chapters in this dissertation. Chapter 2 introduces the sand tank experiment and shows the property estimation of its flow model (for reservoir simulations) and acoustic model (for seismic ray tracing); these properties are needed for building the reservoir simulation models and seismic ray tracing models. Chapter 3 mainly includes the definition of capillary transition zone length and the results obtained from scaling analysis of the capillary transition zone; two

new dimensionless numbers are introduced, capillary number and dimensionless capillary length; the scaling analysis results help us find a proper flow rate for the sand tank experiment. Chapter 4 discusses how the capillary transition zone affects the first arrival of seismic data and shows how to improve the reservoir model by integrating first arrival of seismic data. Chapter 5 gives detailed description of Ensemble Kalman Filer method and the workflow of history matching by using production data and first arrivals of seismic data. Chapter 6 analyzes the production and seismic data from the first sand tank experiment and integrates the production data into the sand tank models to get a better understanding of EnKF behaviors. Chapter 7 introduces the experiment setup, sensor calibrations and data collections in the second sand tank experiment and shows the result of production data integration. Chapter 8 presents the conclusions and further work.

Chapter 2
Sand Tank Transport and Acoustic Properties

Although well logging, well testing and seismic data can be used to estimate formation and fluid properties (Thulin et al., 2007; Li et al., 2009; Valestrand et al., 2010; Dong, 2005), it is still hard to know what the properties of the subsurface are exactly. Theoretical models and reservoir simulators are widely used to simulate the fluid flow in porous media, but there are few data that can be used as a benchmark to verify these models and simulators. Many methods have been advanced to optimize reservoir management, but few of them have been verified with real case studies. The sand tank experiment is a mid-scale experiment which is flexible, repeatable and easy to manage. The data that the "sand tank" produces can be used to verify simulators and optimization methods (Lorenzo et al., 2013).

For the reservoir simulation, the sand tank mass transport properties are required. For seismic ray tracing, the sand tank acoustic properties are required. This chapter mainly discusses how to calculate these properties and what values should be used. A brief introduction to the sand tank experiment is also presented.

2.1   Sand Tank Experiment Description

A flow and seismic experiment is being conducted at the wave tank facility (Coastal Studies Institute of Louisiana State University), here known as the "sand tank". The tank measures approximately 9 m × 6 m on the sides and 0.65 m in height and can be filled up to the desired depth with water and sand. The tank contains a slightly heterogeneous sand pack (two layers of well-sorted, medium-size grains; Table 2.1) that acts as a reservoir. The sand pack in the tank has a trapezoidal cross–section. The top of the trapezoid is two meters long and the bottom is six

TABLE 2.1. Measurement results of sand tank grain size (Smolkin, 2011). The first three samples were collected from upper layer, and the others were collected from the lower layer.

No.	Krumbein Phi Scale	Mean Diameter (mm)	Sorting
Sample 1	1.39	0.38	0.47
Sample 2	1.19	0.43	0.38
Sample 3	1.55	0.35	0.47
Sample 4	1.71	0.31	0.43
Sample 5	1.71	0.31	0.43
Sample 6	1.69	0.31	0.47

meters long. The sand tank is configured with five wells, a production well and four monitoring wells (Figure 2.1). The production well also serves as a monitoring well. Each well is lived with a slotted PVC pipe, so that liquid can pass through and be pumped out of the sand tank, but the sand can not. A large volume of liquid is needed in the experiment. Water is the preferred liquid, because it is safe, inexpensive, and has stable properties at ambient conditions (Smolkin, 2011).

The water table of the sand tank is stabilized at our designed depth (18 cm deep below the surface of the sand) before the experiment. As the water is removed from the sand tank by the production well, the water table falls, and causes changes in the bottom hole pressure of all wells and in the seismic velocity distribution affecting the seismic data collection. This experiment provides observations of production and seismic data from a repeatable, two – phase, meter scale "unconsolidated sand reservoir" for continuous reservoir model updating (Fig. 2.2).

Six sand samples in different parts of the sand tank were selected to calculate the mean and standard deviation of the grain sizes. The first three were from the upper part of sand tank, and the other three were from the lower part of sand tank. They were analyzed by Amy Spaziani of the Coastal Studies Department at LSU for grain sizes (Smolkin, 2011). The grain analysis result (Table 2.1) shows that the grain sizes of lower layer are finer than the ones of upper layer and the

FIGURE 2.1. Sand tank experiment site (Chollett, 2012). Pressure and temperature sensors are placed at the bottom of each well (A, B, C, D and E). Pressure is also monitored in the open–water region of the wave tank; this provides the boundary condition at the sediment–water interface. A flow meter measures the rate from the production well (C). A seismic source (H) with eight accelerometer receivers (I) is set up on the top of the sand to provide seismic data. All data are saved in two nearby computers (F and G) and then forwarded to high performance computers for data processing and reservoir history matching.
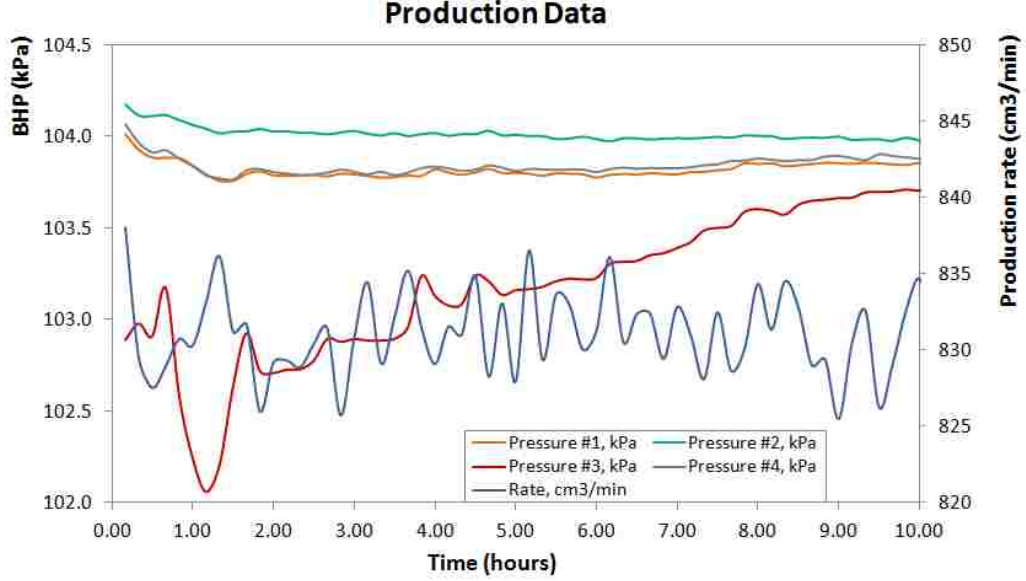
FIGURE 2.2. Sand tank experiment production data (Chollett, 2012). The blue curve marks production rate, and the red one marks bottom hole pressure of the production well. All the other curves indicate the bottom hole pressures of monitor wells. Sensor outputs are converted from volts to p, T, and q in the data acquisition software.

mean grain sizes of upper layer vary by up to 20% while the mean grain sizes of lower layer do not vary by more than 2%. The relation between the Krumbein φ scale (Krumbein and Aberdeen, 1937) and particle diameters are expressed by the following equation:

$$\varphi = -\log_2 d. \tag{2.1}$$

where φ is the Krumbein Phi scale and d is the diameter of the particle (units in mm).

For the sand tank flow model, capillary pressure curve, absolute permeability and relative permeability curve are derived based on the grain sizes.

2.2 Flow Model Properties

For the flow simulation of the sand tank experiment, we need to assign sand and fluid properties. Some properties have constant values and are well documented, such as viscosity, density and compressibility. Some are not, such as capillary pres-

sures and permeabilities; their values are calculated by empirical formulas or as-
signed by using results from experiments on similar sands.

2.2.1 Capillary Pressure Curve

The capillary pressure curve is important in models for the sand tank; it is used to
calculate the initial water saturation under the assumption of equilibrium between
capillary forces and gravity. Relative permeability can be derived from capillary
pressure curve also. During production, the capillary pressure also affects the well
performance.

The experiment performed by Engle et al. (2005) used the Hostun Sand, which
has $\bar{d}_g$=0.355 mm (Lauer and Engel, 2005). Because the average grain size in our
experiment is similar to Hostun Sand (0.35 mm; Table 2.1), their measurement of
the capillary pressure is used in the sand tank model.

The relative permeability and water saturation can be linked by simple, concep-
tual capillary models. The van Genuchten model (Genuchten, 1980) is used here to
fit the capillary pressure data, which can be used to derive the relative permeability
curve. The van Genuchten equation is

$$S' = [1 + (\alpha Pc)^n]^{-l}, \tag{2.2}$$

where α, n, l are constant values determined by curve fitting, and P_c is the capillary
pressure. S' is the effective saturation and it is defined by,

$$S' = \frac{S - S_{wi}}{1 - S_{wi}}, \tag{2.3}$$

where S is the water saturation and S_{wi} is irreducible water saturation. The least–
squares fit of the Hostun sand capillary pressure with the van Genuchten equation
yields parameter estimates $l = 0.65$, $\alpha = 4.56$ psi^{-1} and $n = 5.69$ (Fig. 2.3). The

coefficient of determination (R^2) is 0.9975 which provides an acceptable initial specification for the flow model.
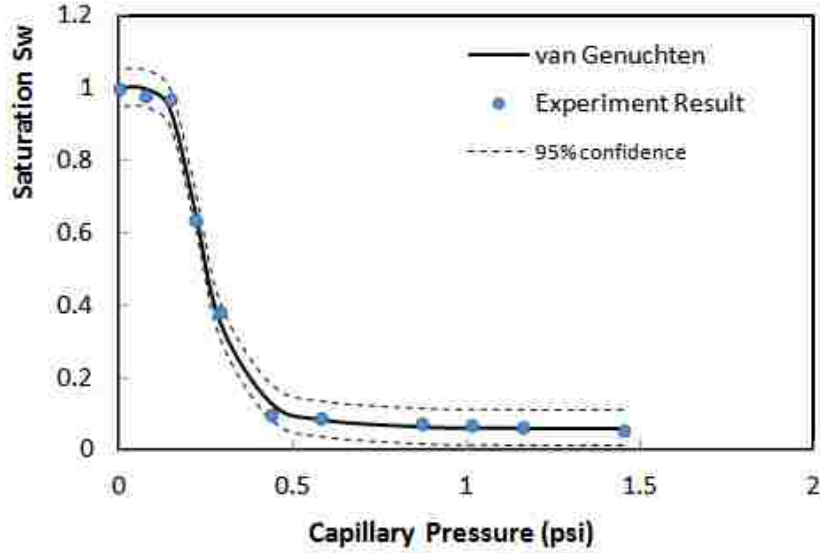

FIGURE 2.3. Measurement and fitting results of the capillary pressure curve. The black solid curve shows the best fitting result according to the van Genuchten equation and the blue circles indicate the experiment data. The dash lines are the 95% confidence interval. The curve fitting is done for the saturation because the pressure goes to infinity when saturation approaches to zero.

For a given type of rock or sediment, the capillary pressure curve changes with varying permeability, porosity and wetting properties. The Leverett J-function is widely used to scale capillary pressure. The Leverett J-function is a dimensionless function describing the relation between water saturation and capillary pressure (Leverett, 1941). Leverett originally attempted to convert all capillary pressure data to a universal one for all k, ϕ, and γ, but that is generally not possible if the rocks or sediment (e.g., sand) have different structures (i.e., are different facies). However, the Leverett J-function has proven valuable for correlating capillary pressure data within one rock type (Collins, 1976). The Leverett J-function is

$$J(S_w) = \frac{P_c(S_w)}{\gamma \cos \theta} \sqrt{\frac{K}{\phi}}. \tag{2.4}$$

19

where γ is surface tension and θ is the contact angle. Based on this J-function, we can calculate the capillary pressure curve of similar porous materials with different grain size and porosity. The Leverett J-function will be used in Chapter 3 for scaling analysis.

For the sand tank flow model, the initial saturation distribution is determined by the capillary pressure curve and the water table level (Fig. 2.4, the depth of free water level is 18 cm).

2.2.2 Permeability

Permeability is the capacity of a porous medium (such as rock, sediment or soil) to transmit a fluid. There are three types: absolute permeability, effective permeability and relative permeability (Ahmed, 2010). Absolute permeability is the permeability measured at 100 percent saturation of that fluid; effective permeability is the permeability measured at a partial saturation with that fluid; relative permeability is the ratio of effective permeability and absolute permeability.

Absolute permeability can be calculated by the Carman–Kozeny equation (Dullien, 1979),

$$k = \frac{d_g^2 \phi^3}{72\tau(1-\phi)^2},\tag{2.5}$$

where k is the absolute permeability, d_g is the grain size, τ is the tortuosity of the medium and ϕ is the porosity. The Carman–Kozeny equation is valid for both rock and sediment (Sprunt et al., 1993).

According to Panda and Lake (1994), the tortuosity is between 2 and 3 in most permeable media with a relatively large permeability, so a tortuosity of 2.5 is used here for the sand tank model. From the Equation 2.5 we know k is inversely proportional to τ and permeability increases with porosity (Figure 2.5) when porosity is in the range of $[0.2, 0.4]$.
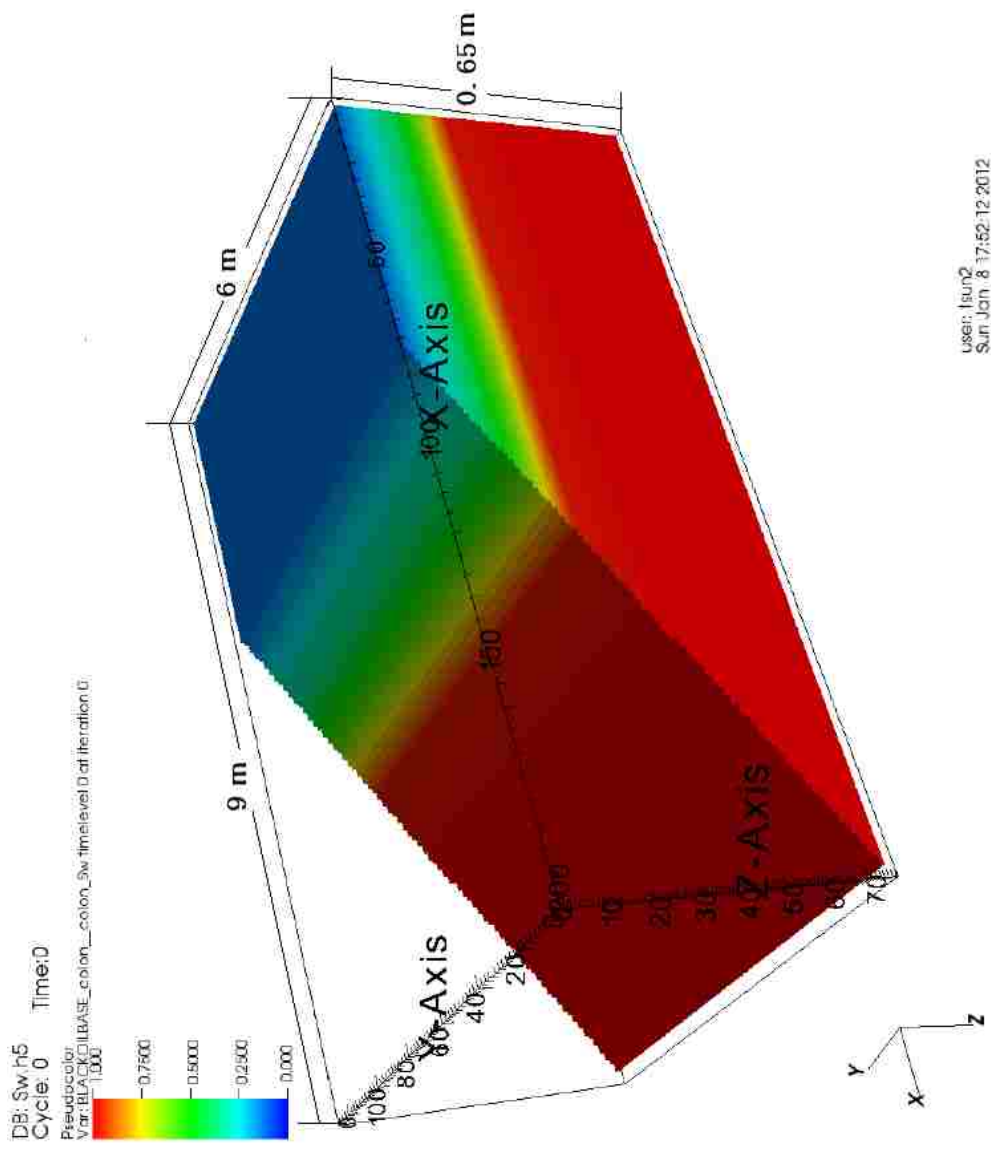
FIGURE 2.4. Initial water saturation distribution of the sand tank model. The X, Y and Z axes are the grid block numbers; the dimension is 9 m × 6 m × 0.65 m with the water table at 0.18 m deep; the saturation distribution is determined by water table level and capillary pressure curve.
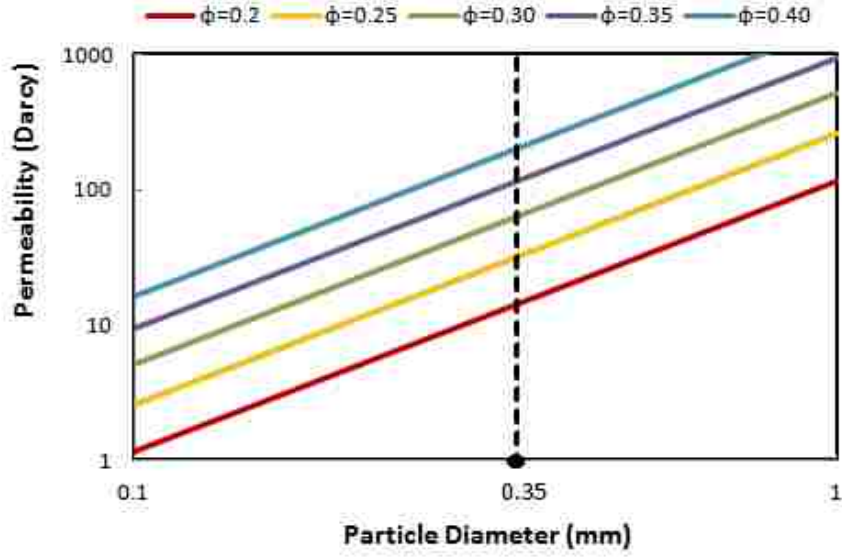
FIGURE 2.5. Absolute permeability changes with different porosities and particle diameters (Assuming $\tau = 0.15$). The intersections of the black dashed line and the other lines show the permeability values of 0.35 mm particle diameters.

Various of models have been used for predicting the relative permeability curve, and they can be separated into two main groups (Mualem, 1976). In the first group, relative permeability is a power function of the effective saturation S'. In the second group, the capillary pressure curve is used to derive relative permeability. Since no measured relative permeability data are available for the sand tank but a capillary pressure curve has been obtained, and Burdine's equations (Amyx et al., 1960) (in the second group) are used to model relative permeability in this study.

$$k_{rw} = \left(\frac{S_w - S_{wi}}{1 - S_{wi}}\right)^2 \frac{\int_{S=0}^{S=S_w} dS/P_c^2}{\int_{S=0}^{S=1} dS/P_c^2}, \qquad (2.6)$$

and

$$k_{rg} = \left(\frac{1 - S_w - S_{rg}}{1 - S_{wi} - S_{rg}}\right)^2 \frac{\int_{S=S_w}^{S=1} dS/P_c^2}{\int_{S=0}^{S=1} dS/P_c^2}, \qquad (2.7)$$

where k_{rw} and k_{rg} are the relative permeability to water and to air, and S_w, S_{wi} and S_{rg} are water saturation, irreducible water saturation and the lowest gas saturation at which the gas phase does not flow.

If van Genuchten's equation is used to relate capillary pressure and water satu-
ration, assuming $S_{rg} = 0$ and $n = 2/(1 - l)$, Burdine's equation can be simplified
to:

$$k_{rw} = S'^2[1 - (1 - S'^{1/l})^l], \tag{2.8}$$

and

$$k_{rg} = (1 - S')^2(1 - S'^{1/l})^l. \tag{2.9}$$

For the relative permeability curve used in the sand tank reservoir model (Figure
2.6), m, n and α are needed; the values of them are derived by fitting the capillary
pressure curve. S_{rg} and S_{wi} are 0 and 0.06 respectively, both of which are read
from the capillary curve.
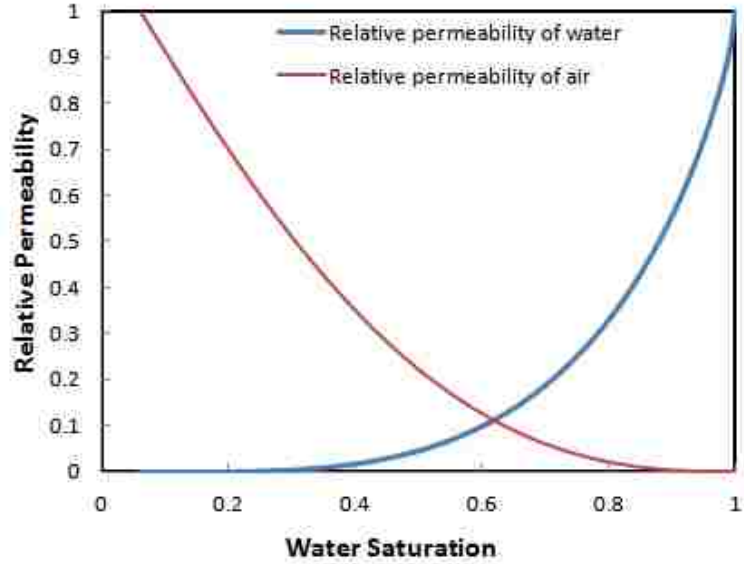

FIGURE 2.6. Relative permeability curves of the sand tank model. They are calculated
by Genuchten's equation.

2.3 Acoustic Model Properties

Ray tracing is used to simulate seismic wave propagation, which depends on the
medium velocities. Density and elastic moduli are used to calculate the velocity
which is affected by the minerals in the grains, the number of grain–to–grain con-

tacts (coordination number), degree of compaction, Poisson's ratio and the saturation. In the sand tank experiment, all these parameters are considered as constants except saturation. The saturation dependence may allow inference of fluid content from seismic responses.

2.3.1 Gassmann Equation

Elastic wave velocity can be expressed as:

$$V_p = \sqrt{\frac{\bar{K} + \frac{4}{3}\bar{G}}{\bar{\rho}}}, \tag{2.10}$$

$$V_s = \sqrt{\frac{\bar{G}}{\bar{\rho}}}, \tag{2.11}$$

where V_p is the compressional wave, V_s is the shear wave, $\bar{K}$ and $\bar{G}$ are the effective material bulk and shear moduli respectively, and $\bar{\rho}$ is its bulk density. The general linear stress-strain relations for a porous elastic solid with fluid were derived by Biot (1956a, 1956b). At its low–frequency limit, Biot's theory relates saturated elastic constants to the material properties as given by Gassmann equation (Gassmann, 1951):

$$\frac{K_{sat}}{K_0 - K_{sat}} = \frac{K_{dry}}{K_0 - K_{dry}} + \frac{K_{fl}}{\phi(K_0 - K_{fl})}, \tag{2.12}$$

$$G_{sat} = G_{dry}, \tag{2.13}$$

in which G_{dry} and K_{dry} are the dry framework shear and bulk moduli, respectively, K_0 is the mineral bulk modulus, K_{fl} is the pore fluid bulk modulus, and G_{sat} and K_{sat} are the saturated effective bulk moduli, respectively. Some assumptions are involved in the derivation and application of Gassmann's equation (Wang, 2001; Dong, 2005):

1. The rock is homogeneous and isotropic.

2. The pores are well connected.

3. Wave frequency is low (close to zero).

4. Viscosities of the fluids are negligible.

5. There is no chemical reaction between the fluid and rock frame.

The assumptions above are generally fullfilled in the sand tank experiment. The sands are unconsolidated and have similar grain sizes, high permeability and porosity. The fluid used here is water, so assumptions 1, 2 and 4 are satisfied; for assumption 3, the frequencies applied in the experiment are not low, but they are less than the high frequency limit (Mavko et al., 1998), and in the seismic data we collect, no dispersion is found, so here we consider assumption 3 is satisfied as well. Assumption 5 is satisfied, because the quartz is not reactive with these fluids at the experimental temperature and pressure. For rocks packed with water and air, the effective bulk modulus of the pore fluid is the harmonic average of the air bulk modulus K_{air} and the water bulk modulus K_{water} (Bachrach et al., 1998b),

$$\frac{1}{K_{fl}} = \frac{S_w}{K_{water}} + \frac{1 - S_w}{K_{air}}, \tag{2.14}$$

where S_w is water saturation of the pore space.

The bulk density is related to saturation and porosity,

$$\bar{\rho} = \phi \left[S_w \rho_{water} + (1 - S_w) \rho_{air} \right] + (1 - \phi) \rho_g. \tag{2.15}$$

$$\bar{\rho} = \phi \left[S_w \rho_{water} + (1 - S_w) \rho_{air} \right] + (1 - \phi) \rho_g. \tag{2.16}$$

in which ρ_{air} and ρ_{water} are the gas and the liquid densities, respectively, and ρ_g is the grain density. By using the formulas above, seismic properties for ray tracing can be derived from the saturation information of flow simulation results. The following shows the steps to calculate the velocities:

- calculate K_{fl} based on equation 2.14

- calculate $\bar{\rho}$ based on equation 2.15

- calculate K_{dry} and G_{dry} based on Hertz-Mindlin Theory

- calculate K_{sat} and G_{sat} based on equation 2.12 and 2.13

- calculate V_p based on equation 2.10

2.3.2 Hertz-Mindlin Method

The Hertz-Mindlin method (Bachrach et al., 1998a) is widely used to calculate elastic velocities of sand. It gives the relationships between the effective bulk and shear moduli for a dry, dense, random pack of identical spherical grains subject to effective stress, and includes the effect of coordination number, and the radius of contact.

$$K_{HM} = \left[\frac{z^2(1-\phi)^2 G^2}{18\pi^2(1-\nu)^2} p_{eff} \right]^{\frac{1}{3}}, \tag{2.17}$$

and

$$G_{HM} = \frac{5-4\nu}{5(2-\nu)} \left[\frac{3z^2(1-\phi)^2 G^2}{2\pi^2(1-\nu)^2} p_{eff} \right]^{\frac{1}{3}}, \tag{2.18}$$

where K_{HM} and G_{HM} are the Hertz-Mindlin effective bulk modulus and shear modulus, z is the coordination number, ϕ is the porosity, G is the shear modulus of grains, ν is Poisson's ratio and p_{eff} is the effective stress. Bachrach et al. (2000) report Poisson's ratio and coordination number of 0.25 and 5 from measurements and interpretations of seismic experiments on a beach. These values will be used to compute the initial guess of acoustic properties in the sand tank experiment, then we will adjust these data to match our observations. Figures 2.7 and 2.8 show the relationship between velocity and saturation based on the Hertz-Mindlin method and the Biot-Gassmann theory, assuming that other parameters are constant. For

low saturations, the velocity decreases as saturation increases. Above a water saturation of 96 percent, the velocity begins to increase. The velocity increases sharply when the saturation is higher than 99 percent.
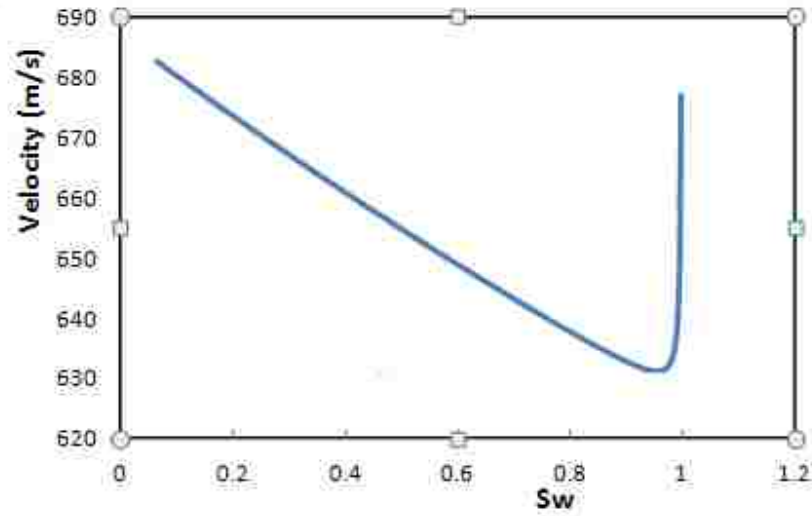

FIGURE 2.7. Saturation versus velocity by Gassmann theory, Biot equation and Hertz–Mindlin method. The velocity is calculated when the saturation is in the range between 0.06 and 0.99, and all the other parameters, such as coordination number and porosity, are constant.

In general, the effective stress is defined as

$$p_{\text{eff}} = p_{\text{total}} - \alpha_b p_{\text{pore}}. \tag{2.19}$$

where p_{total} is the total overburden pressure, α_b is the Biot coefficent, and p_{pore} is the pore fluid pressure, assuming that hydrostatic pressure equals the overburden pressure. For the dry sand, we use $p_{eff} = (\rho_g - \bar{\rho})gZ$, where Z is the depth. The velocity increases with depth because the effective stress increases, but the influence of effective stress on velocity decreases with depth (Figure 2.9).
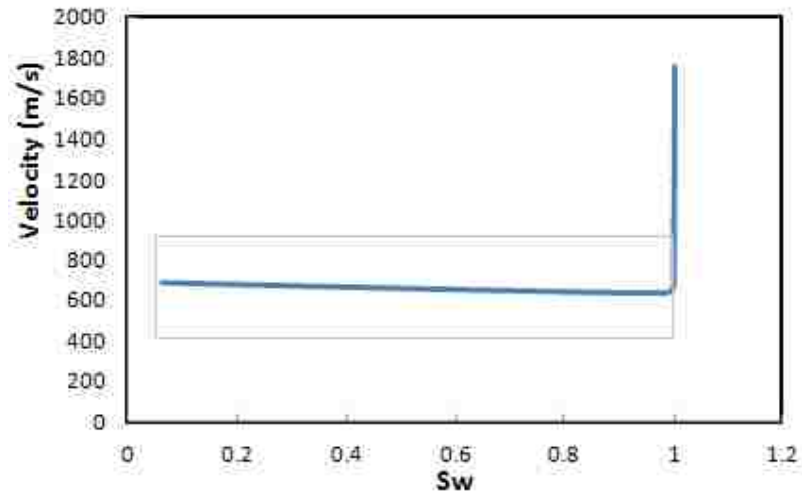
FIGURE 2.8. Saturation versus velocity calculated by Gassmann theory, Biot equation and Hertz-Mindlin method. The velocity is calculated when the saturation is in the range between 0.06 and 1. Compared with figure 2.7, the velocity increases rapidly after the saturation hits 0.99. The lavender rectangle in the background indicates the saturation range for the previous figure (Figure 2.7).
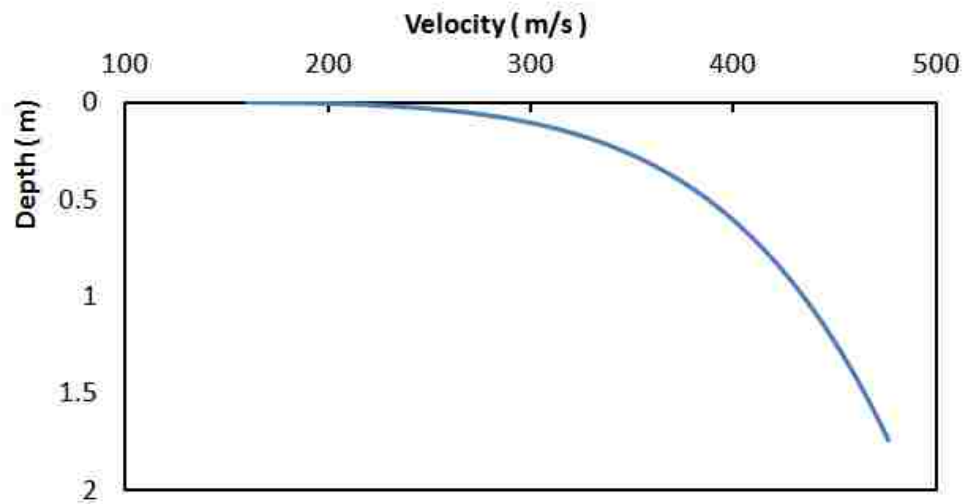

FIGURE 2.9. Velocity versus depth in dry sand by Hertz-Mindlin theory. All parameters are constants except the effective stress on the grains, which increases with the depth. The velocity also increases with the depth.

Chapter 3
Scaling Analysis for Transition Zones

This chapter presents scaling analysis to examine how the thicknesses of capillary transition zones changes during production. Fluid is constrained to flow in a vertical one–dimensional water–air system in a homogeneous porous media (unconsolidated sand), in which the models have sufficient thickness so that the capillary transition zone is small in comparison to the reservoir. The definitions of low and high saturation boundaries are given in this chapter. Thirty models are run for the scaling analysis, and their results allow (1) prediction of the transition zone thickness in large scale (more than 10 m thick) aquifers and (2) selection of a proper flow rate for the sand tank experiment, which will be discussed in the last part of this chapter.

3.1 Dimensionless Formulas

Scaling analysis reduces the number of model parameters to several dimensionless groups, and is used to characterize similar behavior among different models when their dimensionless groups are the same. For experiments and simulations, and can reduce the number of runs and for an actual field study, it can avoid unit conversion (such as, between SI and Field units; Shook et al., 1992).

Shook et al. (1992) defined the gravity number as

$$N_g = \frac{k_z k_{rw}^{\max} \Delta \rho g cos\alpha}{\mu_w u_T} \frac{h}{L},$$ (3.1)

and the capillary number as

$$N_{Pc} = \frac{k_{rw}^{\max} \gamma cos\theta}{\mu_w L_f u_T} \sqrt{\phi k_z},$$ (3.2)

In the above equations, u_T is superficial velocity, which equals the injection or production rate divided by the area; h is the total reservoir thickness; L is the reservoir length; k_z is the vertical permeability; $k_{rw}^{\max}$ is the maximum relative permeability of water; $\Delta\rho$ is the density difference between water and air or water and oil; g is the gravitational acceleration; α is the reservoir dip angle; μ_w is the water viscosity; γ is the water/air interfacial tension; θ is the contact angle; ϕ is the reservoir porosity and L_f will be defined later.

Because we only consider the vertical flow in our scaling analysis, h/L is neglected, and the new formula for the gravity number is:

$$N_g = \frac{k_z k_{rw}^{\max} \Delta\rho g}{\mu_w u_T}, \tag{3.3}$$

The capillary length (dimensionless transition zone length) is defined as:

$$\ell_D = \frac{\ell}{\ell_C}, \tag{3.4}$$

where ℓ_D is the capillary length, ℓ is the transition length during flow and ℓ_C is the transition zone length for the static condition.

In unconsolidated sand, the absolute permeability can be calculated by Carman-Kozeny equation (Eq. 2.5). Because the length of the capillary transition zone changes with time, here the time t is introduced into the capillary number formula by defining:

$$L_f = u_T t, \tag{3.5}$$

where t is the cumulative time since flow began. The new expressions of gravity and capillary numbers are:

$$N_g = \frac{k_{rw}^{\max} \Delta\rho g \phi^3}{72\tau\mu_w(1-\phi)^2}\frac{d_g^2}{u_T}, \tag{3.6}$$

and

$$N_{P_c} = \frac{k_{rw}^{\max}\gamma\phi^2}{\sqrt{72\tau}\mu_w(1-\phi)}\frac{d_g}{u_T^2 t}, \tag{3.7}$$

30

here it is assumed that $k_{rw}^{\max}$, ϕ, $\Delta\rho$, g, α and μ_w are constants, and their values are provided in Table 3.1.

Because the length of capillary transition zone changes with time, a new term t_D is introduced and defined as capillary time, which equals to the reciprocal of the capillary number:

$$t_D = \frac{1}{N_{P_c}}. \tag{3.8}$$

Capillary time will be analyzed in the following sections which will show how the capillary lengths change with capillary time and gravity number.

3.2 Definition of the Transition Zone Boundaries

The capillary transition zone in the water–air system is defined as the interval between the water–air contact (where $P_c = 0$) and the level where irreducible water saturation is present. Both water and air may flow in the transition zone (Ahmed, 2010).

In many reservoirs, the capillary transition zone is important for reserve estimation and connate water distribution modeling. However, the boundaries of the capillary transition zone are not well defined – especially for transient (time–varying) transition zones. Larsen et al. (2000) explained that because the function of the capillary pressure curve is asymptotic towards the irreducible water saturation, it is difficult both theoretically and practically to define the low–saturation boundaries of transition zone. Their research also provided a definition of the transition zone boundaries for the oil–water system, which can be extended to a water-air system. They specified a value ϵ for the derivative of saturation with pressure; the highest point with $\frac{dS}{dP_c} > \epsilon$ is defined as the low–saturation boundary of the capillary transition zone. Because the high–saturation boundary (in exploration and production, the oil–water contact or OWC) is diffuse, this boundary of the transition zone is commonly defined by the free water level (FWL) where the capillary pres-

sure is zero. However, this definition is inaccurate, because in a water-wet reservoir the high–saturation boundary is above the FWL, and in an oil–wet reservoir the high–saturation boundary is below the FWL. In this chapter, for the scaling analysis, a new definition of the low-saturation and high–saturation boundaries of the capillary transition zone is introduced.

3.2.1   Low–Saturation Boundary

For the water–air system, gas is distributed unevenly as it enters the pore space. If the capillary pressure increases, more gas will enter the pores. When the capillary pressure reaches a certain level, the gas will be broadly distributed in the pore space and large pores that dominate fluid flow will become interconnected. In other words, most gas can flow at this saturation, which is defined as the low-saturation boundary of transition zone. Moreover, there is a consistent way to find this low–saturation boundary from the capillary pressure curve based on Swanson (1981)'s paper.

In Fig 3.1, the air–liquid residual–initial saturation (CCI) curve increases almost "linearly" first, and begins to "bend" when the initial saturation reaches 40 percent. At nonwetting saturations less than the "bend" value, the nonwetting phase is easily trapped because it is discontinuous ($S_{nwr} = S_{nwi}$). Trapped saturation falls below the initial saturation for nonwetting saturations greater than the "bend" point, because the nonwetting phase is more continous. The first "bend" is therefore a sensible, nonarbitrary choice for the low–saturation boundary of the capillary transition zone. Upon examination of many CCI and capillary pressure curves, Swanson (1981) stated that the tangent point of a 45–degree line on log–log plot (point A, Fig. 3.2) has the same saturation as the first "bend" point. According to Swanson's conclusion, the low–saturation boundaries can be found easily on capillary pressure curves.
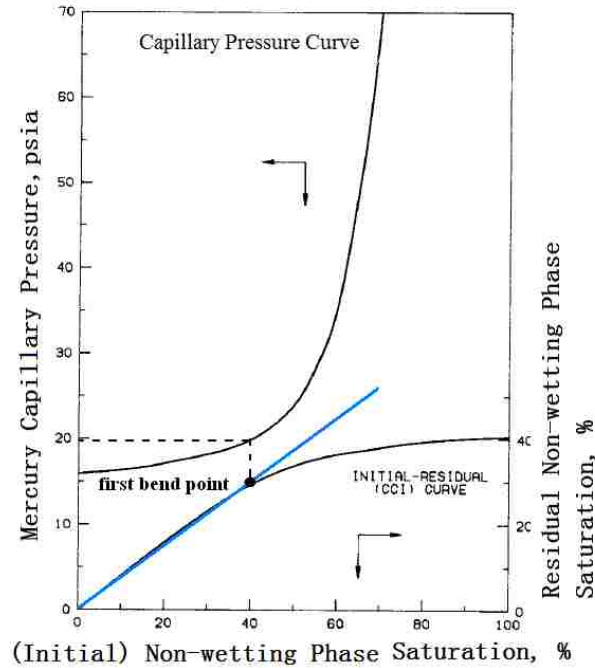
FIGURE 3.1. The two curves shown are (1) hypothetical capillary pressure curve and (2) CCI curve (Swanson, 1981). The blue line is a straight line through the origin with a slope near unity, and helps locate the first bend point. The solid black circle marks the first bend point and the saturation is defined as the low saturation bound.

3.2.2 High-Saturation Boundary

The average water saturation at the breakthrough is used as the high-saturation boundary of the capillary transition zone. This saturation can be found by using Welge's method. Leverett (1941) formalized the analysis of fractional flow. For horizontal flow, and neglecting capillary pressure, the fractional flow of water in a gas-water system is,

$$f_w = \frac{1}{1 + \frac{\mu_w}{\mu_g} \frac{k_{rg}}{k_{rw}}} \, . \tag{3.9}$$

where f_w is the fraction flow of water; μ_w and μ_g are the water viscosity and gas viscosity; k_{rg} and k_{rw} are the relative permeability of gas and water.

Welge (1952) showed that the average saturation after breakthrough can be obtained by laying a tangent line on the fraction flow curve (Figure 3.3); this is a graphical material balance.
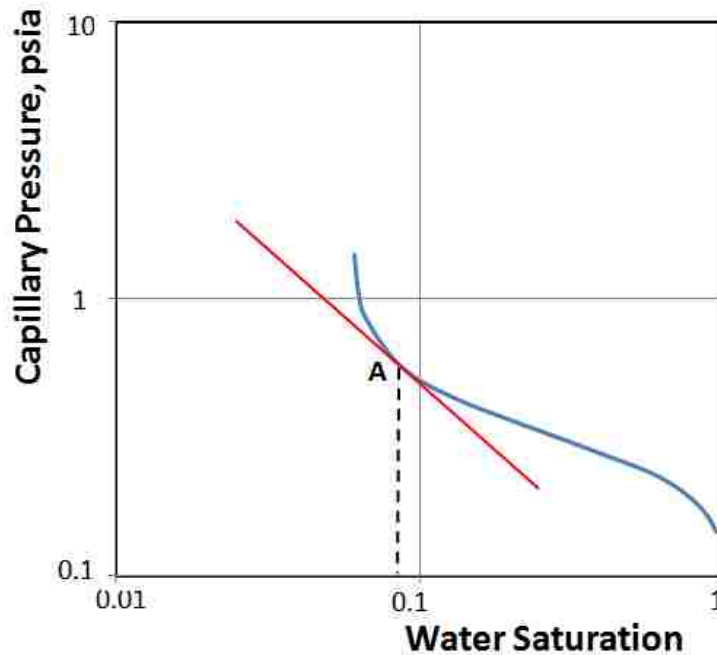
33

FIGURE 3.2. Low-saturation boundary is located by using the Swanson method. The capillary pressure curve is drawn in log–log scale. The 45–degree line (red) is the tangent line to the capillary pressure curve (blue) and A (black) is the point of tangency. The saturation at point A is used as the low-saturation boundary.

3.3   Description of Flow Models

Numerical simulations are used to find the relationship between capillary length, capillary time and gravity number. Fluid flow simulations are performed in a vertical homogeneous model. In this dissertation, flow simulations are separated into two groups—downward flow and upward flow, because different flow directions have different effects on the capillary transition zone. Downward flow compresses the transition zone and upward flow elongates it.

In downward flow models, air is injected at constant pressure at the top of the model, and water is removed at a constant rate from the bottom of the model. In upward flow models, water is injected at a constant rate at the bottom of the model, and air is produced at constant pressure from the top of the model. Models also have different grain sizes and flow velocities. Three different grain sizes and
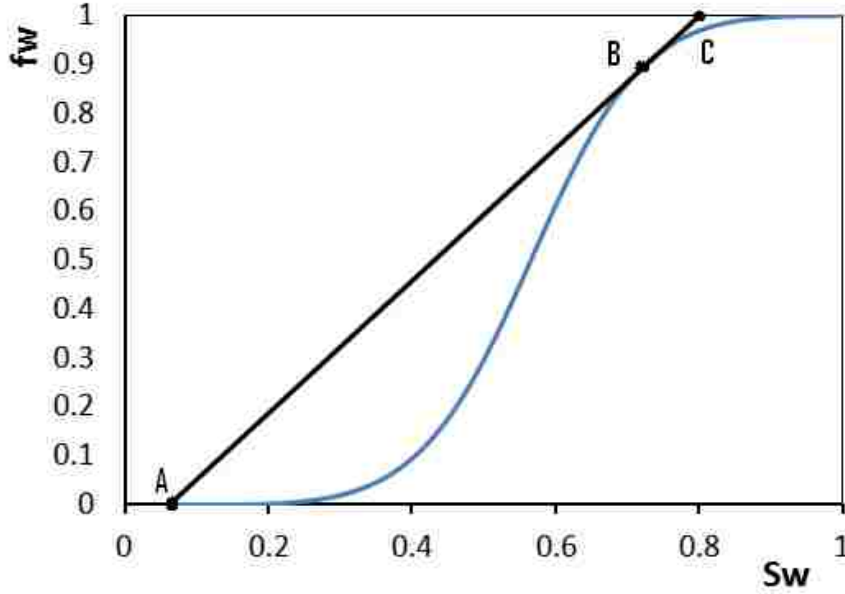
FIGURE 3.3. The high–saturation boundary is located by using the Welge method. A tangent line is drawn from S_{wc} (point A, connate water saturation) to the fractional flow curve (blue line), and the saturation value at the tangent point (point B) is the water front saturation. Extrapolation of this tangent line to $f_w = 1$, intersects point C, which is the average water saturation at breakthrough (Craig, 1975).

five different flow rates are considered (Eqs. 3.10 and 3.11), giving 15 upward flow models and 15 downward flow models for this numerical experiment.

$$d_g \in \{0.15, 0.3, 0.6\} \text{ mm, and} \tag{3.10}$$

$$u_T \in \{0.25, 0.5, 1, 2, 4\} \text{ cm/min}. \tag{3.11}$$

These thirty models are used to confirm that different models (various d_g and u_T) with the same capillary time and gravity number have the same capillary length. In these models, permeability and capillary pressure curves are calculated based on the grain size using the equations in Chapter 2. Other parameters, such as viscosity will be held constant(Table 3.1).

The simulation models are initialized by assuming equilibrium between capillary and gravitational forces and no flow. For each simulation, the transition zone length is recorded at the end of each time step, then capillary lengths, capillary times and gravity numbers are calculated.

TABLE 3.1. Grid and fluid data for the simulations

Grid Count, $x \times y \times z$	$1 \times 1 \times 5000$
Grid Size, $x \times y \times z$	5 cm $\times$ 5 cm $\times$ 2 cm
Porosity (ϕ)	0.35
Water Density (ρ_w)	995 kg m^{-3}
Air Density (ρ_g)	1.16 kg m^{-3}
Water Viscosity (μ_w)	1 mPa·s
Air Viscosity (μ_g)	0.01 mPa·s
Standard Gravity (g)	9.8 m s^{-2}
Dip Angle (α)	0°

3.4 Results and Discussion

In upward flow, the capillary transition zone is compressed and moves upward. In the downward flow, it is elongated and moves downward. At different capillary time, the saturation profiles of the capillary transition zone are different (Figure 3.4). For both upward flow and downward flow, the capillary transition zone is compressed or elongated at lower saturations.

Figure 3.5 shows the scaling analysis results of the capillary transition zone; several features are noteworthy:

- For $N_g > 1$, ℓ_D deviates from 1 at approximately the same t_D in both downward and upward flow.

- For downward flow with $N_g > 1$, after a certain time $\ell_D > 1$ is inversely related to the gravity number. Eventually, $\frac{d\ell_D}{dt_d}$ becomes constant and the transition zone grows linearly for $N_g \geq 1$.

- If $N_g < 1$, downward flow behavior appears to change, but this may be caused by numerical instabilities at high viscous pressure drops or by countercurrent imbibition.

- For upward flow, behavior is similar for all gravity numbers. The capillary length ℓ_D compresses from its static value of 1 over time, and all cases sta-
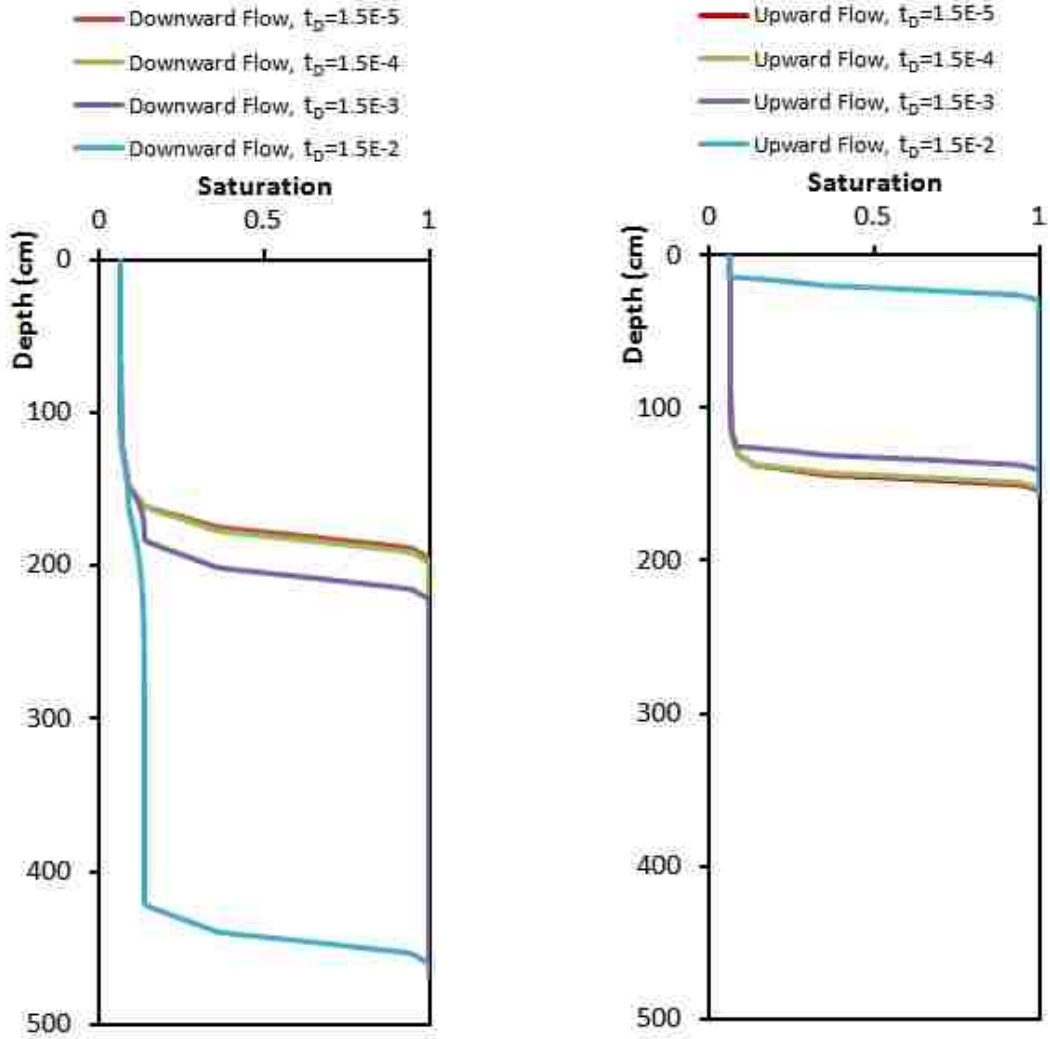
FIGURE 3.4. Saturation profiles for upward and downward flow. The gravity numbers in these two cases are the same, $N_G = 100$. In the downward flow (left), the capillary transition zone is extended and moves downward with production water and in the upward flow (right), it is compressed and moves upward with injecting water.

bilize at some $\ell_D < 1$; the transition occurs later and compression is greater for larger gravity numbers.

In the sand tank experiment, the flow rate is less than 1 gal min^{-1} (6.3×10^{-5} m^3 s^{-1}). Based on Equation 3.1, the gravity number of the sand tank experiment is larger than 260, which is much higher than one. For analysis of the capillary transition zone in the sand tank experiment, results with gravity numbers less
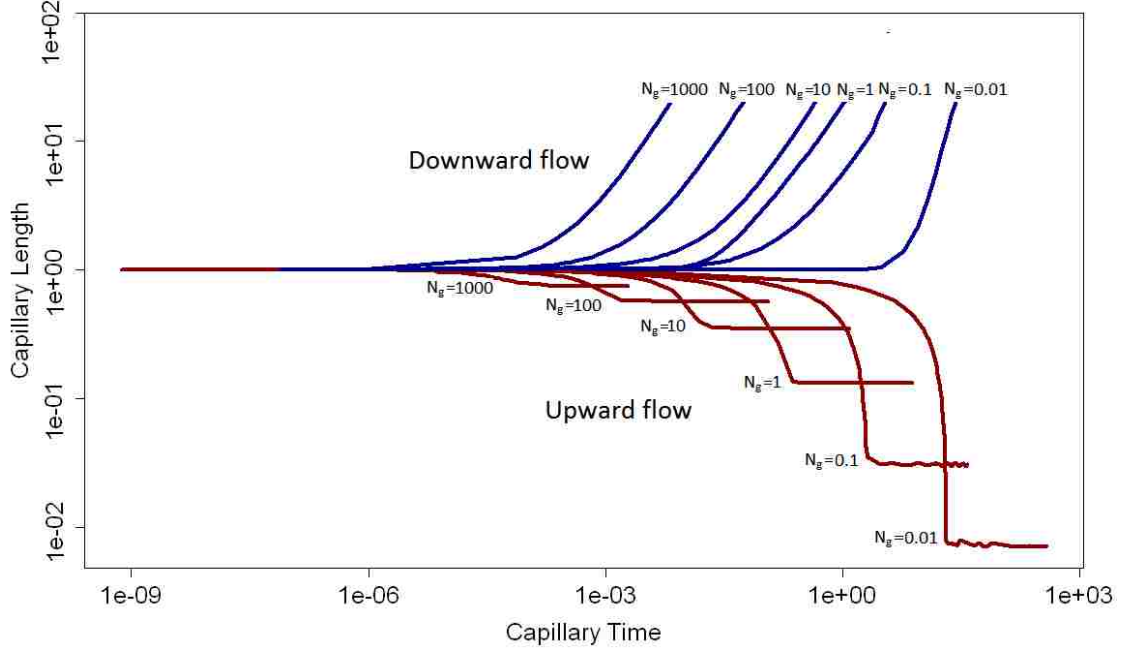
FIGURE 3.5. Dimensionless transition zone length for various capillary and gravity numbers for upward (red) and downward flow (blue). The curves have different gravity numbers and the capillary length changes with the capillary time. The capillary transition zones are compressed in upward flow and extended in the downward flow.

than ten can be neglected. Thus, Figure 3.5 can be simplified to Figure 3.6 and some characteristics are easy to identify for the flows with $N_g > 10$:

- Each curve can be divided into three sections: an initial linear section ($\ell_D = 1$), transition section ($\frac{d\ell_D}{dt_d} \neq$ constant) and final linear section ($\ell_D =$ constant or $\frac{d\ell_D}{dt_d} =$ constant). With increasing N_g, the transition section becomes shorter and the flow enters the final linear section with smaller capillary time.

- For the downward flows with different N_g, the final linear sections are parallel with the same separation distances and the unit slope is close to 1.

- For the upward flows with different N_g, ℓ_D are different constants at the final linear sections, and the compressed length $(1 - \ell_D)$ is nearly halved if N_g
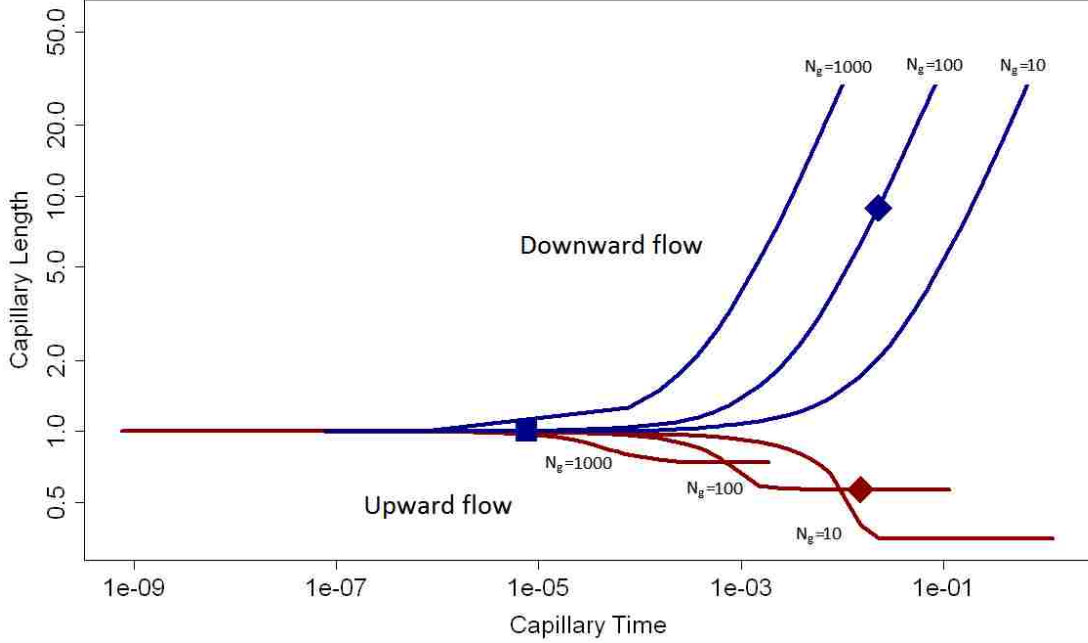
38

FIGURE 3.6. Dimensionless transition zone length for gravity numbers 10, 100, 1000 of upward and downward flow. The water saturation distributions at the three large points are used to calculate the velocity for seismic raytracing in Chapter 4. One case is taken at static conditions, one in stabilized upward flow, and one in pseudostable downward flow.

increases ten times. The curve fitting result shows the relationship between the gravity number and the compressed length,

$$N_g = -0.084 \ln(1 - \ell_D) + 0.838. \tag{3.12}$$

the R^2 is 0.9953

These scaling analysis results provide guidelines for selecting rates and times for the sand tank experiment. First, during the experiment we can estimate the capillary transition zone size using capillary time and gravity number without running a numerical simulation. Second, the scaling analysis results can help us select a suitable flow rate for the sand tank experiment. Because the sand tank has a limited vertical extent compared to the scaling simulations and the capillary transition zone cannot grow or compress to very large or very small values, the

suitable flow rate should keep the transition zone size unchanged for the duration of the experiment. Figure 3.6 shows that the capillary transition zone size does not change when the capillary time is less than 10^{-6}. Using the Equations 3.7 and 3.8, the result shows that a flow rate less than 0.9 gal/min will keep the transition zone size unchanged if the sand tank experiment runs ten hours. At last, the scaling analysis results can be verified by sand tank experiments after setting up the saturation meters.

Chapter 4
Seismic Resolvability of Transition Zones

For a water–air system, the transition zone (water saturation distribution) changes during the production of water and leads to the changes of the velocity distribution, and ultimately affects the seismic arrival times. The effective stress also affects the velocity distribution and seismic arrival times, because effective stress affects the effective bulk modulus and shear modulus. In this chapter, velocity models are calculated at different conditions and seismic rays are traced through these velocity models. The results show that water saturations and effective stresses affect the first arrival times of seismic data.

4.1   Velocity Models

The Hertz-Mindlin and Gassmann equations for calculating velocities have been shown in Chapter 2, and effects of water saturation and effective stress also have been discussed in Chapter 2. The conclusion was that velocity increases with increasing effective stress where velocity decreases with increasing saturation up to 0.99, then the velocity increases sharply at water saturation larger than 0.99 (Figures 2.7 to 2.9). In fact, the water saturation and effective stress both change with depth, and in this chapter effects of that joint variation are assessed, including examples. Parameters used to calculate velocities are given in Table A.2.

In the velocity calculation, effective stress is derived by the formula $\sigma_{eff} = \sigma_{ob} - p_w$ (Chapter 2) to calculate the effective dry bulk modulus and shear modulus (Eqs.2.17 and 2.18). In the sand tank experiment, because σ_{ob} is much larger than p_w, σ_{eff} approximately equals to σ_{ob}. Two velocity profiles are calculated by using $\sigma_{eff} = \sigma_{ob} - p_w$ and $\sigma_{eff} = \sigma_{ob}$ separately. The results (Figure 4.1) show that the

p_w is negligible in the velocity calculations for the sand tank models. The benefit is that dry frame bulk and shear modulus do not need to be recalculated each time, and when the number of grid blocks is large, calculation times can be reduced. However, p_w still can be considered to increase the accuracy.
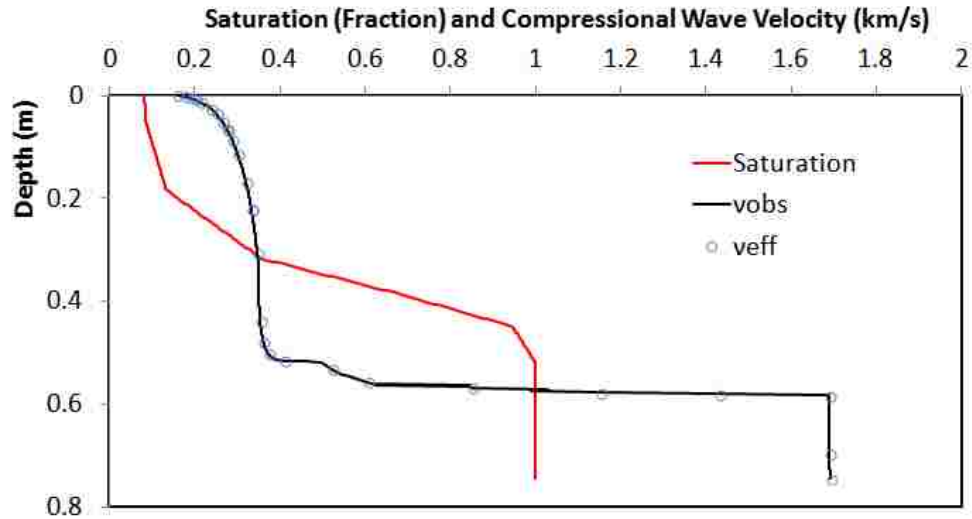

FIGURE 4.1. The velocity profiles for static condition by using two different effective stress formulas. In one case, velocity (v_{eff}) is calculated assuming $\sigma_{eff} = \sigma_{ob} - p_w$ (black curve). In the other case, velocity (v_{ob}) is calculated using σ_{ob} (blue circles). The two velocity profiles are almost the same. The red curve indicates saturation distribution versus the depth.

The effective stress is dominated by the overburden stress, so if the capillary transition zones are at different depths, the effective stresss and velocity profiles will also be different. Figure 4.2 shows the velocity profiles if the same transition zones are at different depths and implies the following conclusions: First, the overburden stress increases the velocity in the transition zone. Secondly, if the effective stress starts from zero (i.e., the section of interest begins at atmospheric pressure, as it does here), a marked velocity increase will be apparent in the shallow part; if not, the velocity profile will remain almost constant until the saturation approaches 1. Thirdly, the saturation dominates as $S \to 1$. The cases examined have different effective stressses, but the velocities change sharply to similar values (1.7 km/s).
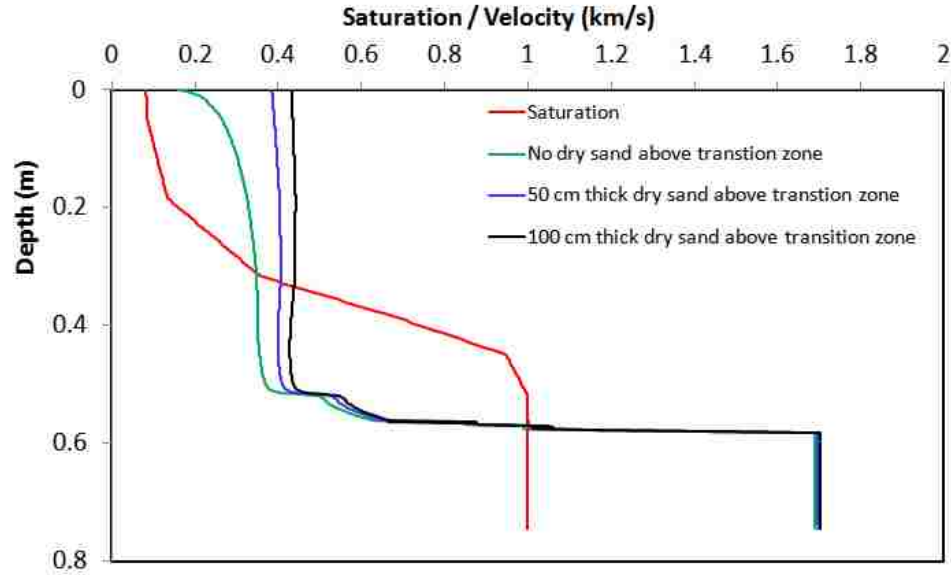
FIGURE 4.2. The comparison of the velocity profiles at static condition with zero, 50 cm and 100 cm of thick dry sand above transition zone. The red curve marks the saturation profile; the green, blue and black curves mark the velocity profile at different conditions. Velocities change sharply to 1.7 km/s when saturation changes from 0.98 to 1 in all three conditions. When saturation is less than 0.98, the velocities are between 0.2 and 0.6 km/s.

Figure 4.3 shows the saturation and velocity profiles under 1) static conditions, 2) condition of upward flow and 3) condition of downward flow for the given capillary times (large points in Figure 3.6). In these three models, it is assumed that the top of capillary transition zone is at the ground surface, so $S = S_{wi}$ and $\sigma_{eff} = 0$ at the top and both of them increase with depth. For these cases, there are two parts where velocity gradient is largest: (1) near the surface (dimensionless depth less than 0.02), because the effective stress starts from zero; and (2) in the vicinity of the water table (dimensionless depth between 0.82 and 0.85) because the water saturation approaches to 1. In the middle part of the transition zone (dimensionless depth between 0.02 and 0.82), with both saturation and effective stress increasing, their opposing effects on velocity cause the velocities to increase only slightly with depth. For the downward flow condition, with the depth increasing and elongated transition zones, the saturation affects velocity more than effective stress does: in

this case, there is an interval of dimensionless depth (0.83 to 0.85) in which velocity decreases.
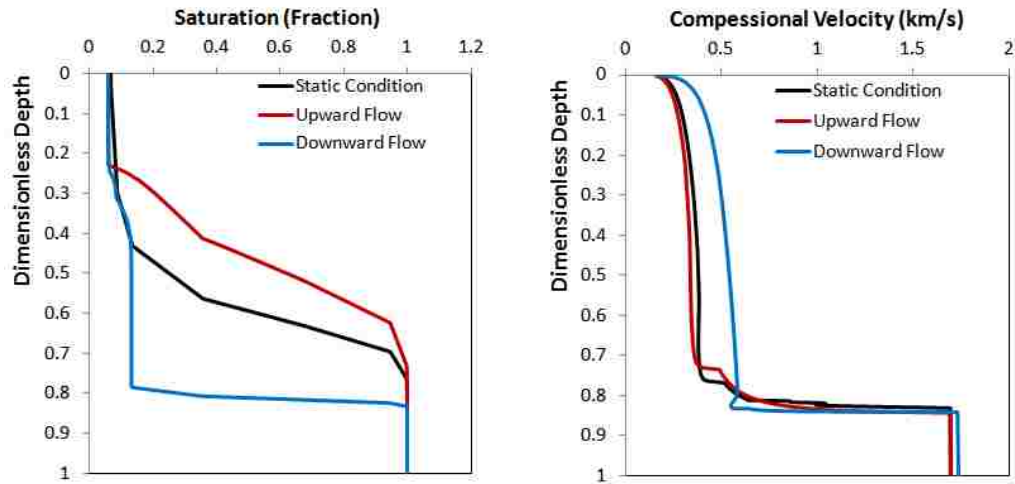
(a) Saturation profiles

(b) Velocity profiles

FIGURE 4.3. The saturation and velocity profiles under different conditions. The black curves indicate a static condition, the red curves indicate the upward flow and the blue curves indicate the downward flow. The dimensionless depth is defined by the actual depth divided by its transition zone size. (a) Upward flow compresses the saturation transition, and downward flow elongates the transition. (b) The velocity profiles are calculated based on their corresponding saturation profiles.

4.2 Raytracing Results

To test the seismic resolvability of the capillary transition zone, seismic ray are traced through the different velocity models (Figure 4.3). Because these velocity models are only in one dimension (vertical), and the raytracing has to run in a 2-D model, the velocities are assumed to be constant horizontally. In the raytracing, the seismic source was placed at the left side on the surface and the receivers were put in a line to the right side of seismic source. The raytracing software used here is the open source program RAYINVR (Zelt, 1988) and it assumes that the wave frequency is infinite.

Figure 4.4 shows the wave paths of raytracing results, saturation and velocity profiles. The 2-D velocity models are discretized into several constant–velocity

44

layers as indicated by the dashed horizontal lines. Because the velocity gradient is larger near the surface and near the water table, these regions are discretized more densely than other regions. The three raytracing results have several similarities. Because the velocity variation is large in the region near the surface and the region near the water table, most of the waves are refracted from these two regions. The refracted waves from the near surface region can be received by most of the receivers because the waves get refracted without traveling a long distance. The refracted waves from the near water table region cannot be received by the receivers close to source because the waves must travel a long distance with a small incidence angle to get refracted. In the intermediate region (between near–surface region and water table), few waves are refracted, because the velocity variation is small in this region and only waves with large incidence angles can be refracted. A comparison the three wave paths in Figure 4.4, if the water table is deeper, the receivers should be placed further from the source to detect the refracted waves. This conclusion can help with seismic experiment design.

Raytracing (Figure 4.5) computes the arrival times of the waves. If the water table is deep enough, the first arrivals of waves are waves refracted from all regions (near–surface region, intermediate region and water table). If the water table is shallower, then first arrivals are mainly waves refracted from regions near the surface and water table. There is a crossover point at which the first arrival waves change from near–surface waves to ones that travel near the water table. This point moves toward the seismic source when the water table moves up. With different water table levels, the seismic first arrival times are very different.
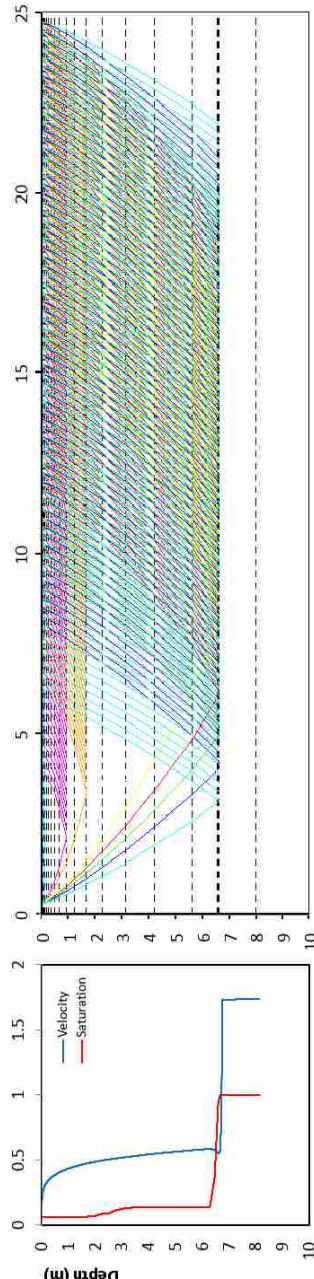
4.3   Conclusions

In this chapter, the Hertz-Mindlin theory and Gassmann equations are used to calculate the velocity models under different conditions (static, upward flow, and
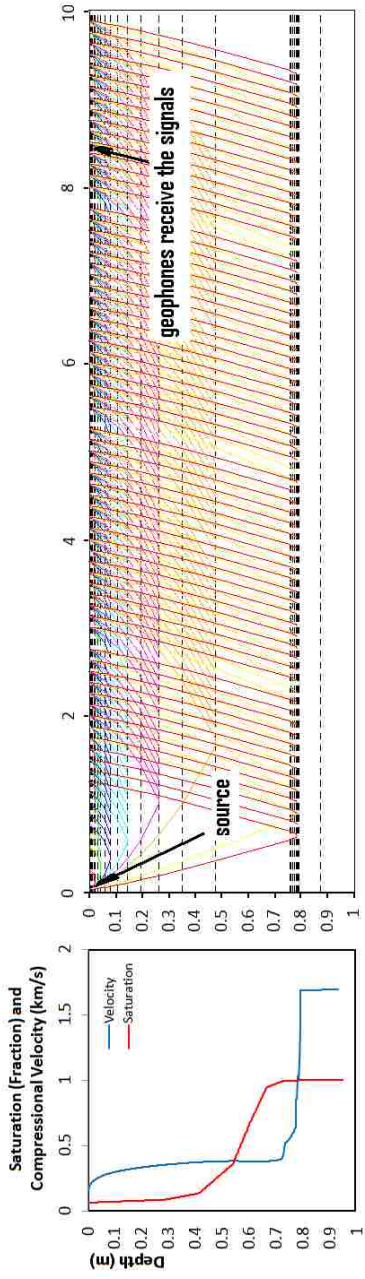
(a) Saturation profile, velocity profile and ray path under static condition
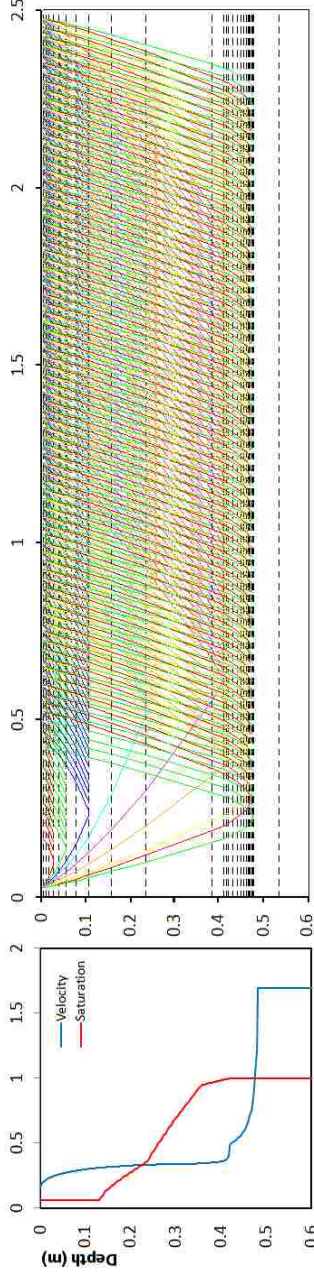
(b) Saturation profile, velocity profile and ray path under upward flow condition

(c) Saturation profile, velocity profile and ray path under downward flow condition

FIGURE 4.4. The left subfigures show the saturation and velocity profiles in three different conditions. The velocities increase near the surface and in the water table region. The right subfigures show the paths of refracted waves through the 2-D velocity models. The source is at the left corner and the seismic receivers are placed in a row on the surface, extending to the right. The velocity models are discretized into several layers based on the velocity variation (dashed horizontal lines in right figures).

downward flow). The results show that: 1) there are two regions in the sand tank model where that velocity gradient increases sharply. One is near the surface and caused by low effective pressure; the other one is near the water table and caused by water saturation approaching to 1. 2) Effective stress affects the velocity profile, but its influence becomes weaker as effective stress increases.

Seismic raytracing based on velocity models for three saturation profiles (static, upward flow, and downward flow), indicates that the water table is the main factor affecting first arrival times by affecting the water saturation distribution. With a shallower water table level, first arrival times will be earlier. When the water table level is shallow, most of the seismic first arrivals are refracted wave from the regions near the surface and water table. With the water table getting deeper, some seismic first arrivals are refracted waves from the intermediate region. In another word, the velocity profiles in the intermediate region also affect the seismic first arrival times. Since the velocity is determined by water saturations and effective pressures, we can conclude the seismic first arrival times are affected by water saturations and effective pressures, so it is reasonable to attempt to integrate them to decrease flow model uncertainty.
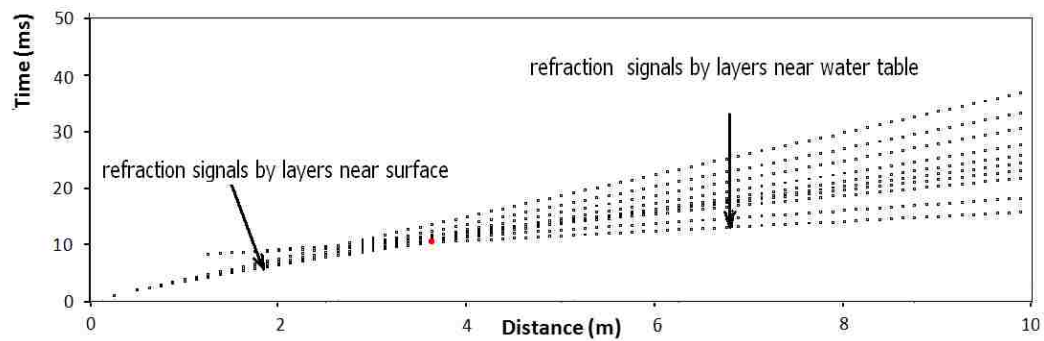
(a) Refracted wave arrival time of the model in static condition
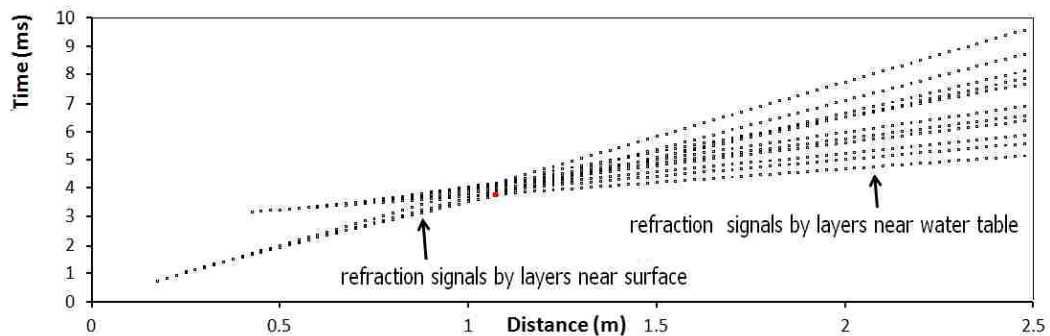
(b) Refracted wave arrival time of the model in upward flow condition
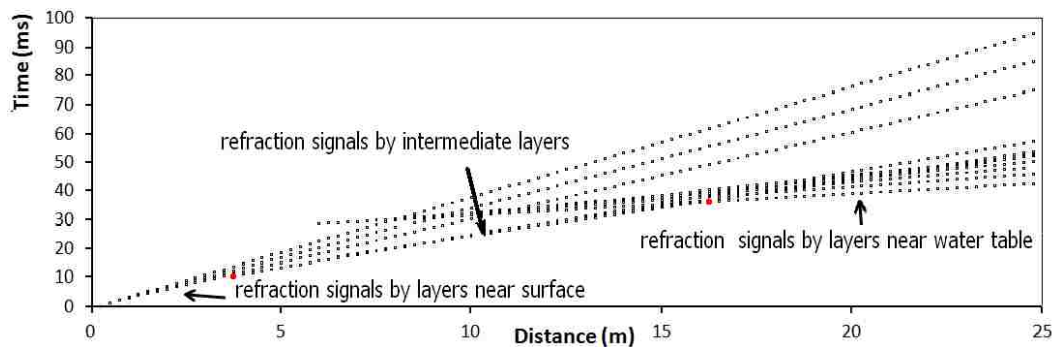
(c) Refracted wave arrival time of the model in downward flow condition

FIGURE 4.5. Raytracing estimates the time that the refracted waves arrive at different receivers. In the static condition and upward flow condition, the first arrivals are the waves refracted by the regions near surface and water table. In the downward flow condition, some of first arrivals are the waves refracted by the intermediate regions because the water table is far away from the surface. The red points are the crossover points of shallow versus deep waves.

Chapter 5

Workflow for Integration of Sand Tank Experimental Data via the EnKF method

Reservoir history matching is a process to minimize the differences between observed data and simulation results. In this work, the ensemble Kalman Filter method is selected as the history matching method to integrate the production data of sand tank experiment. For a better understanding of the EnKF method, its advantages and formulas will be described in this chapter, and a continuous reservoir model updating workflow to integrate the sand tank experiment data will also be described including the extra steps for integrating seismic first arrival data. Then, methods to include capillary pressure, relative permeability and compressibility in the history matching process are discussed. Finally, unconditional simulation is introduced to initialize the ensemble of models.

5.1 Ensemble Kalman Filter

The Ensemble Kalman Filter method is a Monte Carlo implementation based on Bayesian theory. It is initialized by generating an ensemble of models based on prior information. The models are typically evolved through time using numerical methods and are updated whenever new observations are available. The updating step is based on Bayesian theory to balance deviations from the prior model with residuals versus predicted simulation results, and obtain improved estimates of model parameters (Oliverbook et al., 2008). The EnKF method has following advantages compared with other methods:

- The formula of the EnKF method is straightforward and easy to apply, so that there is no need to do complicated coding.

- The EnKF method uses the reservoir simulator as a black box, and only requires the output of simulator. Thus it does not need to access the reservoir simulator code to calculate gradients for history matching.

- The EnKF method allows updating reservoir models sequentially; new data are integrated as they are measured, and earlier data does not need to be matched again. This feature enables continuous reservoir model updating.

- The EnKF method provides uncertainty estimates, because in each updating step the whole ensemble of models is updated and all the models honor the new data.

- The EnKF method can be readily parallelized, because the forward steps in the EnKF method are independent for each member of the ensemble.

To apply the EnKF method, one must first generate an ensemble of reservoir models which is consistent with prior knowledge of the reservoir. We denote a state vector for each reservoir model which combines the following variables and is expressed as,

$$y_j = [(m_j), (f_j), (d_j)]^T, j \in \{1, 2, \ldots, N_e\} \tag{5.1}$$

In the above equation, m is a row vector and denotes the static parameters, such as permeability and porosity; f is a row vector and denotes the dynamic variables, such as saturation and pressure; d is a row vector and denotes the predicted production observations, such as production rate and bottom hole pressure; j is the index of ensemble members and N_e is the number of reservoir models in the ensemble.

The EnKF method consists of two steps: the predicting step and the updating step. In the predicting step, the reservoir simulations are run and the state vectors

(y_j) change from time $i - 1$ to the next time step i:

$$y_{i,j}^p = F(y_{i-1,j}),\qquad(5.2)$$

in which $F()$ represents running the reservoir simulations. The superscript p indicates predicted results, and i is the time step. The differences between $y_{i,j}^p$ and $y_{i-1,j}$ are the residuals with respect to the dynamic variables and the predicted production.

The second step is to update the parameter values of the ensemble members by using,

$$y_{i,j}^u = y_{i,j}^p + K_e(d_{obs,i,j} - Hy_{i,j}^p),\qquad(5.3)$$

where the superscript u indicates update. H is a measurement operator which extracts the simulated data from the state vector and only contains 0 and 1. $d_{obs,i,j}$ is a perturbed observation and K_e is the ensemble Kalman gain, both of which will be explained in the following.

The observations $d_{obs,i}$ are obtained at different time steps i. Because using the same observations for all ensemble members will cause the updated ensemble variance to be very low (Oliver et al., 2008), a random perturbation is added:

$$d_{obs,i,j} = d_{obs,i} + \xi_{i,j},\qquad(5.4)$$

where $\xi_{i,j}$ is the observation error at time step i, and it is assumed to follow a Gaussian distribution with expected value $\langle \xi_{i,j} \rangle = 0$ and covariance $\langle \xi_{i,j} \xi_{i,j}^T \rangle = C_{i,D}$.

$K_{i,e}$ is the ensemble Kalman gain which can be expressed as,

$$K_{i,e} = C_{i,Y} H^T (H C_{i,Y} H^T + C_{i,D})^{-1},\qquad(5.5)$$

where $C_{i,Y}$ is the covariance matrix of the state vector. It is hard to calculate $C_{i,Y}$ directly, but it can be approximated by using the ensemble,

$$C_{i,Y} \approx \frac{1}{N_e - 1} \sum_{j=1}^{N_e} (y_{i,j}^p - \bar{y}_i^p)(y_{i,j}^p - \bar{y}_i^p)^T,\qquad(5.6)$$

where $\bar{y}_i^p$ is the mean of the state vector at time step i before the updating step.

$$\bar{y}_i^p = \frac{1}{N_e - 1} \sum_{j=1}^{N_e} y_{i,j}^p. \tag{5.7}$$

5.2 Workflow of Integrating Sand Tank Experiment Data

According to Eqs. 5.2 to 5.7, a complete workflow (Figure 5.1) for integrating sand tank experiment data is formed as shown:

1. Initialize the ensemble of reservoir models. Because porosity and permeability are the two parameters to be calibrated, all the reservoir models have the same parameters except porosity and permeability. The porosities and grain size distribution of each reservoir model are different, and they are generated using unconditional simulation method (White, 2010). Next, the permeability distribution is calculated based on the Carman-Kozeny equation. The initial pressure and saturation distribution are calculated based on the hydrostatic equilibrium and capillary/gravity equilibrium (Chapter 3).

2. Run the ensemble of reservoir models. Meanwhile, wait for observation data from sensors.

3. Start the sand tank experiment. Turn on sensors and computers to collect the experimental data (bottom–hole pressures, flow rates and seismic arrival times) and the pump to produce the water.

4. When new experiment data are recorded by the sensors and sent to high performance computers, recognize the data type (seismic or production data). If the observation is seismic, an algorithm will will estimate the first arrival time. If it is production data, no algorithm will be applied and the data will be passed directly to the Kalman gain calculation.

FIGURE 5.1. Workflow for data integration into the sand tank model. Production and seismic data are streamed from the sand tank experiment A to the simulator B; some components are executed in parallel, C. There are two loops for sand tank experiment data integration, one is for production data and the other is for seismic data. For seismic data integration, first arrival picking is applied to the observation data and rock model conversion and seismic raytracing are used to calculate the simulated first arrival times.

53

5. Extract the saturations (for computing first seismic arrivals), or well production rates and pressures (for production data). If the data are seismic, calculate the velocity model based on the saturation field (Chapter 3), then run a seismic ray tracing simulation and compute the first arrival time.

6. Based on the mismatch between observations and simulated results, update the ensemble of models by using the EnKF method and then go to step 4.

First arrival times of seismic refraction data are included in this workflow. The approach is innovative in that it integrates the seismic data without a separate seismic inversion, as required in some other data integration approaches (e.g., Kalla et al., 2008; Kalla et al., 2009). The first arrivals are picked from the observed amplitude versus time traces by an automated pick algorithm in Seismic Unix (Center for Wave Phenomena 2012). Meanwhile, velocity models use the Hertz–Mindlin method based on the saturations predicted by the reservoir simulation. Next, the velocity models are used for seismic ray tracing (`FAST`; Zelt, 1988) to provide the simulated first arrival times .

The observed and simulated first arrival times are sent (along with rate and pressure observations) to the EnKF program to update the reservoir models. A localization method is used to improve the stability of the EnKF method (Li, 2008). This method is tested on the sand tank experiment which provides pressure, production rate, and seismic observations.

5.3   Software and Hardware Tools

- Reservoir simulator: IMEX is the reservoir simulator used in this work, and is provided by Computer Modeling Group (CMG). IMEX is a conventional black oil reservoir simulator and can be used to simulate the primary, secondary and enhanced or improved oil recovery processes where changing fluid

composition and reservoir temperature have little effects on accurate modeling of hydrocarbon recovery processes (CMG, 2009).

- Seismic ray tracing: FAST is a program package for 2D and 3D first arrival traveltime tomography. The velocity model and the location of source and receivers are the input, and the output is the first arrival time (Zelt, 1988). The velocity model represents the physical space by an array of discrete cells and only one velocity value is assigned to each cell. The rays travel in straight lines in each cell and are refracted or reflected at the cell's boundary.

- History matching (EnKF) program: see Appendix B.

- All the reservoir simulations, seismic ray tracings and history matchings are run on the supercomputers in LSU. Tezpur is a 360-node cluster with 15.3 TFlops Peak Performance running the Red Hat Enterprise Linux 4 operating system. Each node contains two Dual Core Xeon 64-bit processors operating at a core frequency of 2.66 GHz. Tezpur was delivered to LSU on November 3, 2006 and is open for general use to LSU users (Tezpur, 2013).

5.4 Calibration of Other Fluid Properties in the History Matching Process

To simplify the data integration process in the sand tank experiment, only permeability, porosity, saturation and pressure are calibrated. Other properties such as capillary pressure, relative permeability and compressibility are assumed to be known. However, in some reservoirs, these properties significantly affect the simulation results (Tanaka et al., 2010; Shams et al., 2013; Ghamdi and Ayala, 2010), and some research (Reynolds et al., 2004) has been done to consider relative permeability in reservoir history matching. Additionally, when seismic data are integrated, some rock properties that affect the results are assumed to be known (Dong, 2005),

such as the bulk modulus, shear modulus and coordination number. This section will show how to incorporate the capillary pressure, relative permeability and rock properties into the EnKF formula.

In the section 5.2, the Eq. 5.1 defines the state vector as,

$$y_j = [(m_j), (f_j), (d_j)]^T, j \in \{1, 2, \ldots, N_e\}, \tag{5.8}$$

where m is a row vector that denotes the static parameters. Generally, only permeability, porosity, saturation and pressure (Oliver et al., 2008) are considered, so m is defined as,

$$m_j = [ln(k_j), \phi_j, p_j, (S_w)_j], j \in \{1, 2, \ldots, N_e\}, \tag{5.9}$$

where $ln(k)$ is a row vector of the logarithm of permeability; ϕ is a row vector of porosity; p is a row vector of the pressure and Sw is a row vector of water saturation; If capillary pressure, relative permeability, compressibility and rock properties for seismic data integration are incorporated, the m term will be defined as,

$$m_j = [ln(k_j), \phi_j, p_j, (S_w)_j, (p_c)_j, (k_r)_j, (c_r)_j, (R_{si})_j], j \in \{1, 2, \ldots, N_e\}, \tag{5.10}$$

where p_c and k_r are the row vectors for the capillary pressure curve and relative permeability curve; c_r is the rock compressibility. R_{si} is a row vector for rock properties that affect seismic data integration.

For example, in sand tank model, the capillary pressure curve is defined as,

$$\frac{S - S_{wi}}{1 - S_{wi}} = [1 + (\alpha P_c)^n]^{-l}, \tag{5.11}$$

where P_c is the capillary pressure; S is the water saturation and S_{wi} is irreducible water saturation; α, n, m are the constants used to define the curve shape. In

the formula, it is observed that the capillary pressure curve can be calibrated by changing the values of S_{wi}, α, m and n, so p_c in Eq. 5.10 can be defined as,

$$p_{c_j} = [(S_{wi})_j, \alpha_j, l_j, n_j], j \in \{1, 2, \ldots, N_e\}, \tag{5.12}$$

Relative permeability is defined by Burdine's equation:

$$k_{rw} = (\frac{S - S_{wi}}{1 - S_{wi}})^2 [1 - (1 - (\frac{S - S_{wi}}{1 - S_{wi}})^{1/l})^{(1-2/n)}], \tag{5.13}$$

and

$$k_{rg} = (1 - \frac{S - S_{wi}}{1 - S_{wi}})^2 (1 - (\frac{S - S_{wi}}{1 - S_{wi}})^{1/l})^{(1-2/n)}. \tag{5.14}$$

where l, n and S_{wi} are the same parameters as those for capillary pressure curve, so k_r in Eq. 5.10 can be defined as,

$$(k_r)_j = [l_j, n_j, (S_{wi})_j], j \in \{1, 2, \ldots, N_e\}, \tag{5.15}$$

Shear modulus of grains (G), Poisson's ratio (ν) and coordination number (z) are the rock properties that affect the seismic data integration, so R_{si} is defined as,

$$R_{si} = [G_j, \nu_j, z_j], j \in \{1, 2, \ldots, N_e\}, \tag{5.16}$$

Take the Eqs. 5.12 and 5.16 into Eq. 5.10, then we have

$$m_j = [ln(k_j), \phi_j, p_j, (S_w)_j, (S_{wi})_j, \alpha_j, l_j, n_j, (c_r)_j, G_j, \nu_j, z_j], j \in \{1, 2, \ldots, N_e\}, \tag{5.17}$$

this m_j will be used in the EnKF method which takes the capillary pressure, relative permeability and compressibility into consideration for integrating production data, and grain's shear modulus, Poisson's ratio and coordination number for integrating seismic data.

5.5   Sand Tank Model Initialization

To match the observation data of sand tank experiment, porosity and permeability are the two parameters tuned using the EnKF method. Unconditional simulation (White, 2010) is used here as a geostatistical technique to generate the prior porosity and permeability field, which are used as initial guesses.

Unconditional simulation does not honor individual points, but only the overall mean and variance are used. It has advantages over kriging and other linear interpolation techniques because they maintain the spatial variability of the property being simulated. With the unconditional simulation any number of nonunique realizations or possibilities for the spatial distribution of permeability and porosities can be generated. Based on grain size analyses (Smolkin, 2011), the logarithm of grain sizes are normally distributed with a mean of 1.54 and a standard deviation of 0.2. The porosity is normally distributed with a mean of 0.35 and a standard deviation of 0.025. The cross-correlation coefficient of grain size and porosity is assumed to be 0 (Beard and Weyl, 1973). The variogram is exponential and the range is assumed to be 5 grid blocks. The initial covariance function of porosity and permeability in the three–dimensional grid system are:

$$C_\phi(i_1, i_2) = \sigma_\phi{}^2 exp(-\frac{3|i_1 - i_2|}{a_1}), \qquad (5.18)$$

and

$$C_{ln(d_g)}(i_1, i_2) = \sigma_{ln(d_g)}{}^2 exp(-\frac{3|i_1 - i_2|}{a_1}), \qquad (5.19)$$

where a_1 is the range of variogram, i_1 and i_2 are the location vectors of two grid blocks. The initial covariance function for $ln(d_g)$ is:

The procedures for the property model construction are:

1. construct the covariance matrix C_ϕ and $C_{ln(d_g)}$ using the Eqs. 5.18 and 5.19

2. decompose them using the Cholesky decomposition:

$$C_\phi = L_\phi L^T{}_\phi, \ C_{ln(d_g)} = L_{ln(d_g)} L^T{}_{ln(d_g)}, \tag{5.20}$$

3. generate the porosity field

$$\phi = \mu_\phi - \sigma_\phi L_\phi Z_1, \tag{5.21}$$

where μ_ϕ is the prior mean of porosity and σ_ϕ is the standard deviation. Z_1 is vector of uncorrelated random number with standard normal distribution.

4. generate the grain size field

$$ln(d_g) = \mu_{ln(d_g)} - \sigma_{ln(d_g)} L_{ln(d_g)} (\rho Z_1 + \sqrt{1 - \rho^2} Z_2). \tag{5.22}$$

where $\mu_{ln(d_g)}$ is the prior mean of logarithm of grain size and $\sigma_{ln(d_g)}$ is the standard deviation. Z_2 is vector of uncorrelated random number with standard normal distribution.

5. calculate the permeability using Equation 2.5.

Figure 5.2 and 5.3 are the permeability and porosity distribution of four models picked from the forty initial models. We can see that they have different permeability and porosity distributions.

Two sand tank experiments have been done. One was conducted by Shannon Chollett (2012) and another one was conducted by Ting Sun and Jie Shen. Data from both experiments will be used to test the EnKF method in the following two chapters.

(a) Permeability distribution of Model 10

(b) Permeability distribution of Model 20

(c) Permeability distribution of Model 30

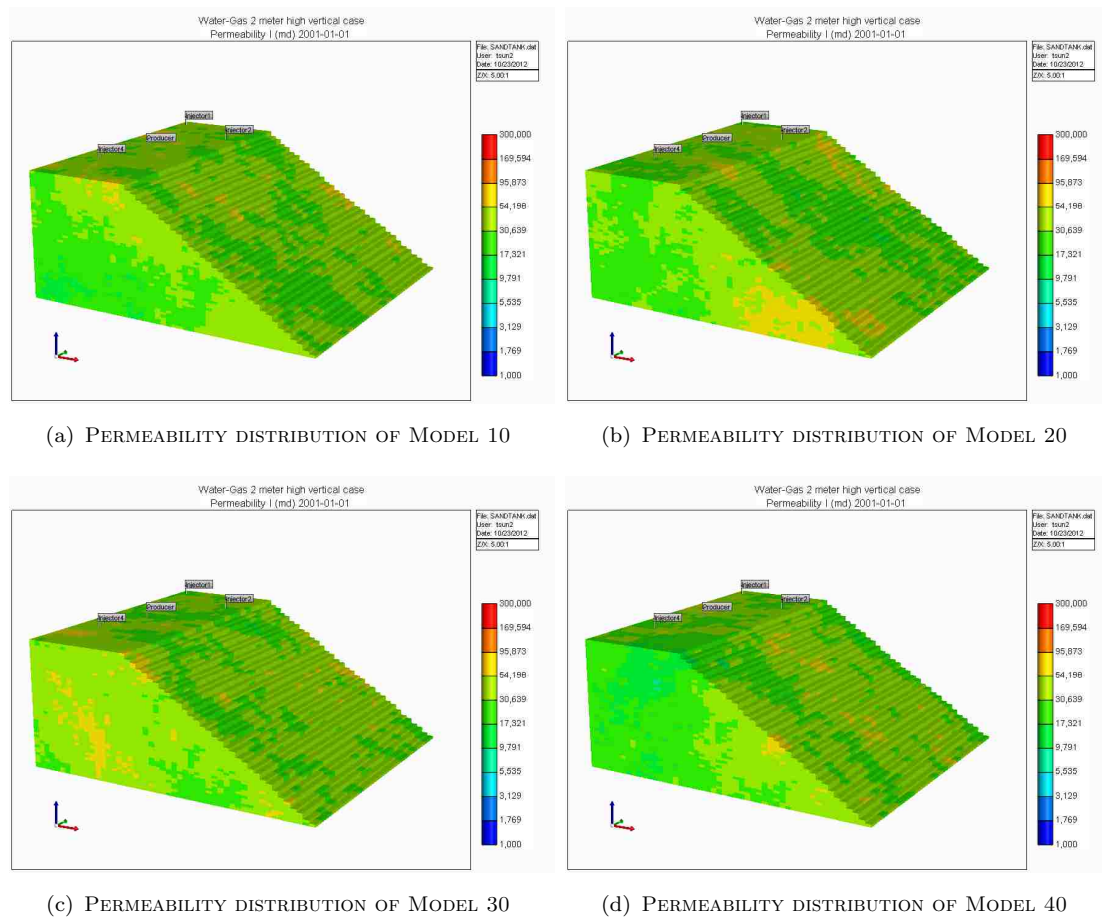(d) Permeability distribution of Model 40

FIGURE 5.2. Permeability of prior models of the second sand tank experiment. Each model has a different permeability distribution and the prior permeability is in the range between 17 darcy and 54 darcy.
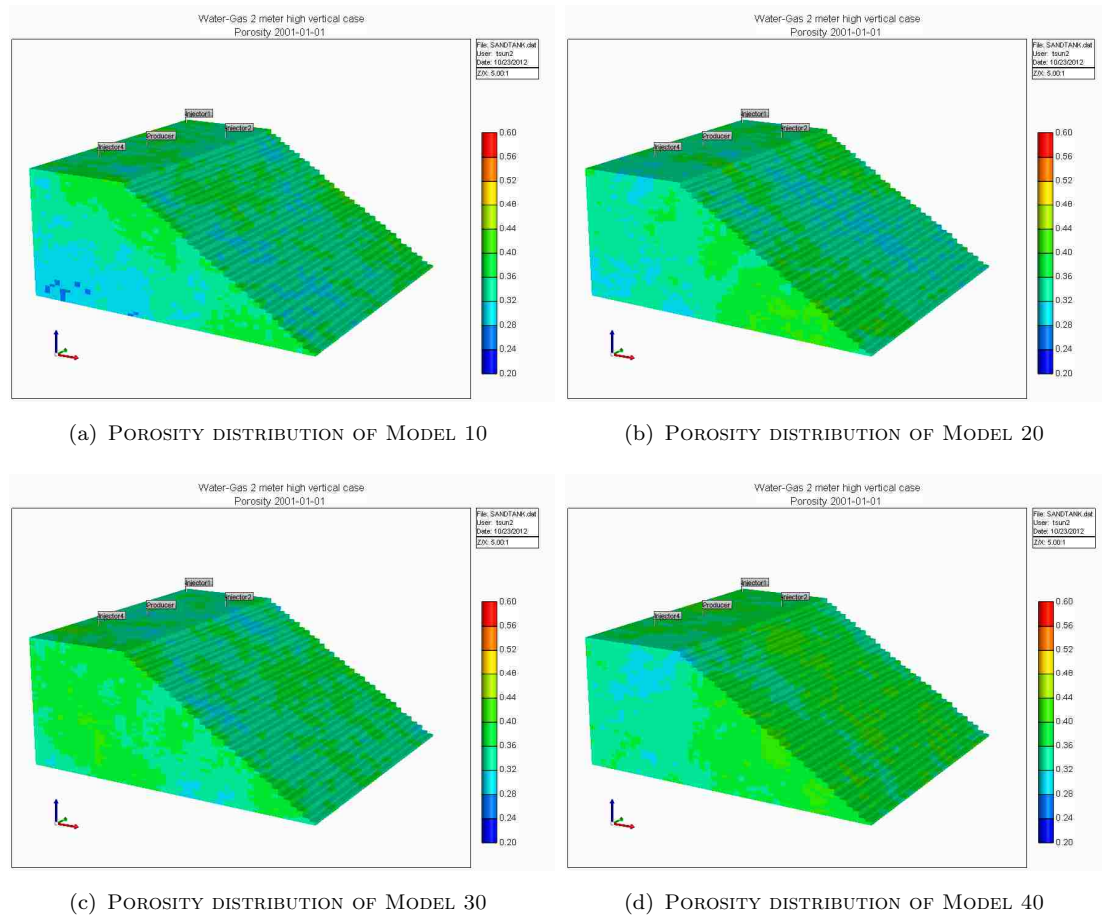
(a) Porosity distribution of Model 10

(b) Porosity distribution of Model 20

(c) Porosity distribution of Model 30

(d) Porosity distribution of Model 40

FIGURE 5.3. Porosity of prior models of the second sand tank experiment.Each model has a different porosity distribution and the prior porosity is in the range between 0.32 and 0.44.

Chapter 6
Analysis and Integration of Experimental Data with Large Errors

6.1 Introduction

Many methods have been developed for continuous reservoir model updating. However, there are few data sets to test the history matching methods. The real field data can be used, but the collection of the field data is time–consuming and expensive and the subsurface data sets are nearly impossible to validate. Comparing with real field, although the sand tank is small (meter scale), it is physical–rich, highly repeatable and has various experimental configurations. So sand tank is more suitable to test the history matching method.

In Chapter 5, EnKF method and data integration workflow have been introduced. In this chapter, both the production and seismic data acquired in the first experiment are analyzed, and integrated with the production data to test the performance of the EnKF method.

6.2 First Sand Tank Experiment

The first experiment was conducted by Chollett (2012), to collect both production data and seismic data. The sand tank was filled with water to a height of 30.5 cm and four wells were placed at different locations to mimic field production behavior. The well in the center was producing water and the other wells were used as the monitoring well. The bottom–hole pressures of all the wells and the flow rate of the water production well were collected every 5 seconds (Figure 6.1), and the seismic data were collected for the dry tank at the beginning of the experiment and one hour and five hours later during the experiment (Figure 6.2). The location

of pressure and temperature sensors and the seismic shots and receivers are shown in Figure 6.3.
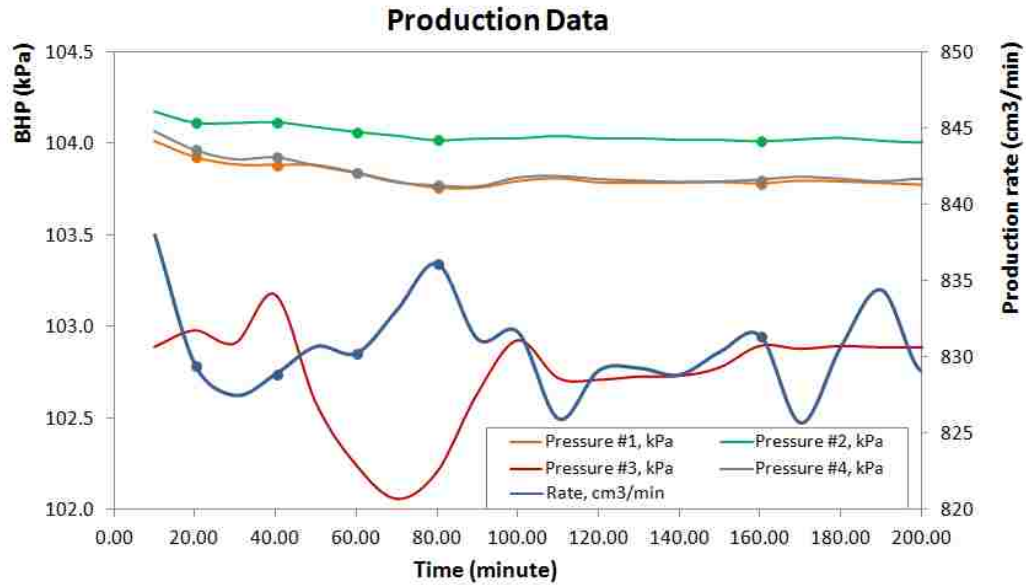

FIGURE 6.1. The red curve indicates the bottom–hole pressure of the production well. Bottom–hole pressure decreased in the beginning and increased after 1 hour production; the blue curve indicates the flow rate of the production well, and it oscillated near 830 cm^3/min; the top curves indicate the bottom–hole pressure of the monitoring wells, and they decreased from beginning to the end, but only a little-less than 0.5 kPa (Chollett, 2012). The circles with solid fills are the integrated production data.

6.3   Production Data Integration

In the real field, the production data are collected routinely and contain information reflecting the reservoir properties, therefore, they are the most frequently used data for history matching.

In this section, the production data of the sand tank experiment will be integrated to improve the sand tank models. Before integration, the sand tank experiment data are analyzed briefly, then a primary history matching is done to obtain a better understanding of the sand tank experiment that the bottom of the sand tank is uneven and corrections should be added to the observed pressures of
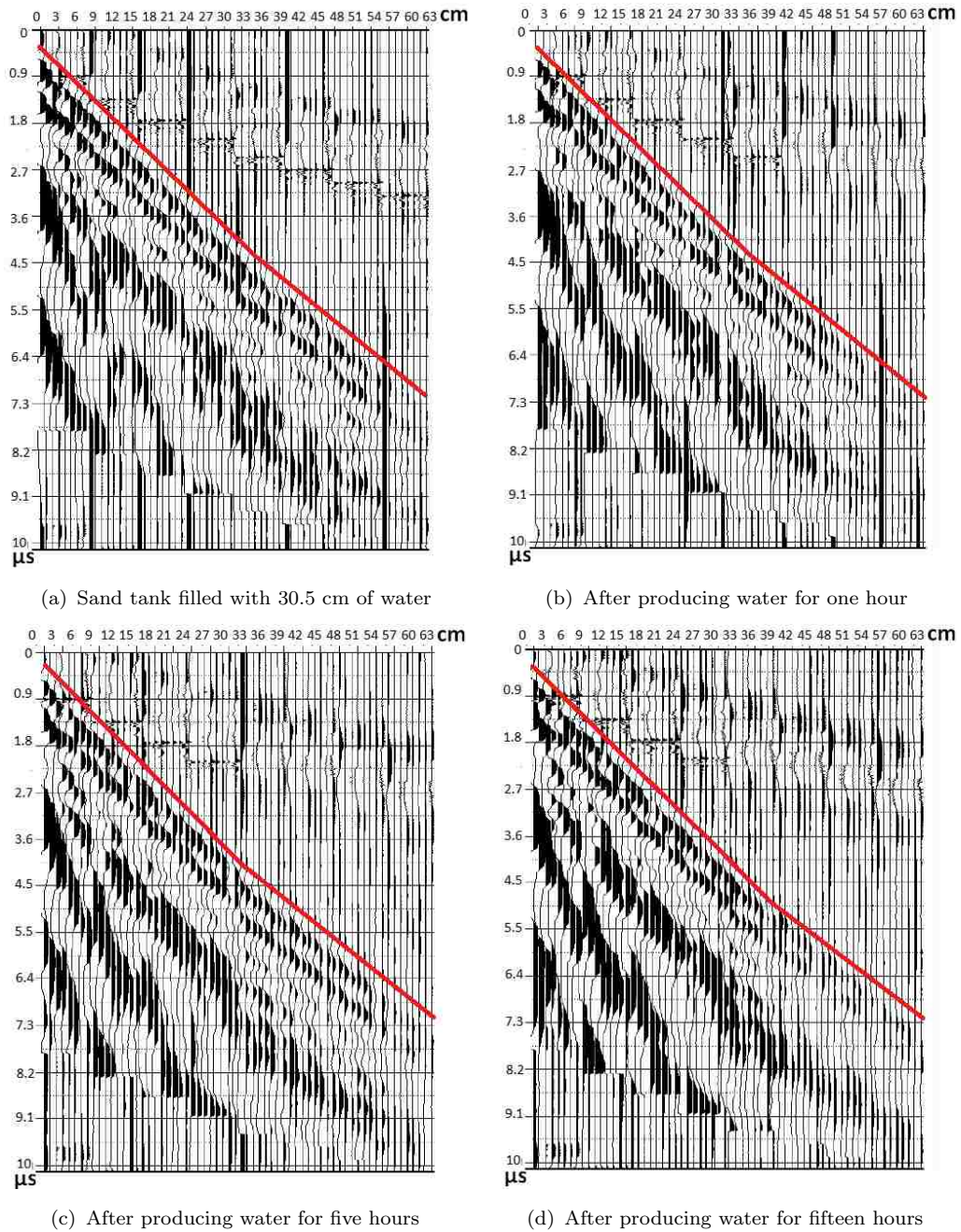
(a) Sand tank filled with 30.5 cm of water

(b) After producing water for one hour

(c) After producing water for five hours

(d) After producing water for fifteen hours

FIGURE 6.2. Seismic traces (amplitue versus time at various receiver locations) of the sand tank at different times (Chollett 2012). The surface waves and some noise from collection equipments are clearly presented. The red lines mark the first arrival data.

the monitoring wells. Lastly, corrections for bottom–hole pressures are applied to obtain an improved history matching.
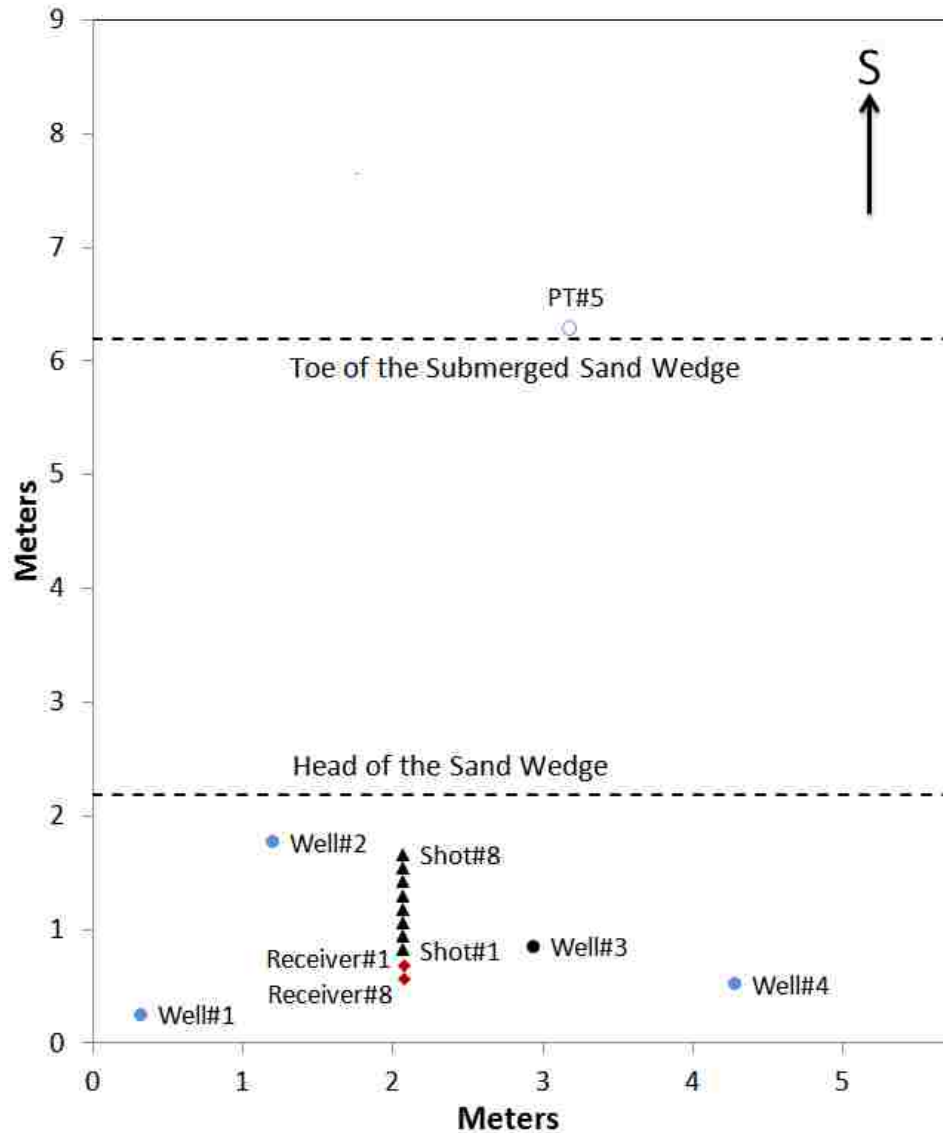
FIGURE 6.3. For the first experiment, well #1, well #2 and well #4 (blue circles with solid fill) were monitoring wells and well #3 (black circle with solid fill) was the production well. Each well had a PT sensor placed at the bottom to record the bottom–hole pressure and temperature. The PT sensor #5 (blue circle without fill) was placed at bottom of the open water area to record the changes of boundary conditions. A pipe joined to a pump was placed in the production well and reaches the bottom, and they were used to produce water from well #3. The seismic shots (black triangles) and receivers (red diamonds) were placed straight in line, and there are receivers 2-7 between receiver 1 and 8. They are not marked because of legibility.

6.3.1 Production Data Results and Analysis

Before integrating the production data, we need to understand and analyze the experimental results (Figure 6.1). The experiment results show that the measured

flow rate of the production well is constant (830 cm^3/min) and that the bottom–hole pressure decreases from 103 kPa to 102 kPa (between 0 and 70 minutes) and increases from 102 kPa to 102.8 kPa (between 70 and 100 minutes). After 100 minutes, the bottom–hole pressure stays constant at 102.8 kPa. The causes of the bottom–hole pressure changes of the production well will be discussed later in this subsection. For the three monitoring wells, the measured bottom–hole pressures decrease first, and then stay almost constant (104.1 kPa for well #2 and 103.8 kPa for well #1 and well #4).

In the sand tank experiment (Chollett 2012), there are three monitoring wells and one production well. A big open water area is on one side of the sand tank, and it is considered as a constant pressure boundary. The top of the sand tank is open to the air, and we can also consider it as a constant pressure boundary. All the other sides are no flow boundaries. Generally, if there is only one production well with a constant flow rate, the bottom–hole pressure of the production well should decrease throughout the experiment. There appears conflict between our analysis and the experiment results of the bottom–hole pressure of the production well.

One possible reason that the bottom–hole pressure increases during the experiment is that the flowmeter used in this experiment was inaccurate (Chollett, 2012). The relative measurement error of flowmeter is 38 percent and the true flow rate is decreasing with time (Chollett, 2012).

Another possible reason for the unusual bottom–hole pressure is the sand migration. The sand is unconsolidated and the slits on the PCV pipe are 0.254 mm thick (Chollett, 2012) which are close to the average grain diameter 0.35 mm (Smolkin, 2011). During production, the grains may move with the water and pack at the wellbore or flow into the wellbore. This will cause a wellbore damage or improve-

ment and can be described by skin effects (Mian, 1992). A positive skin effect indicates wellbore damage and a negative skin effect indicates wellbore improvement. The following section will provide more discussions on skin effects in sand tank experiment.

### 6.3.2 Primary History Matching

Generally, flow rates are used as well control parameters for field operations, since they are much easier to regulate than the bottom–hole pressures and we are interested mainly in flow rates not bottom–hole pressures. Therefore, flow rates are used as well constraints and the bottom–hole pressures are used as observations commonly during the reservoir history matching (Oliver et al., 2008). However, this is not mathematically correct because the flow gauges always have larger measurement errors than the pressure gauges, if they are used as well constraints, a relatively larger error will be introduced into reservoir simulation and the simulation results will not be reliable for history matching. In the first sand tank experiment, since the measurement errors of the flow rate (38 percent) are much higher than the pressure errors (between 2.3 percent and 3.4 percent), the bottom–hole pressures of the production well are used to constrain well conditions. The flow rates of the production well and the bottom–hole pressures of the monitoring wells are used as observation variables in the history matching.

A comparsion of the simulation results of the initial and updated models (Figure 6.4 and 6.5) shows that:
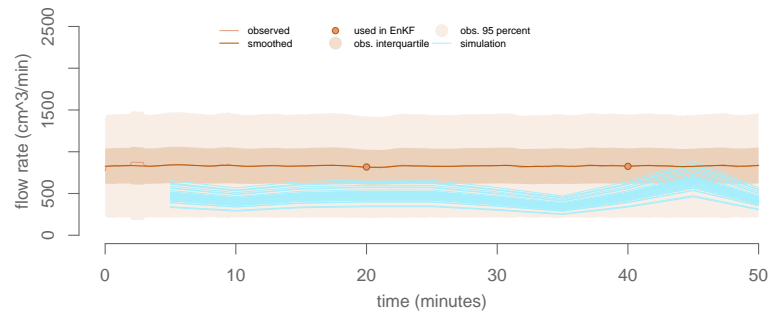
1. The well–flow rates of the initial models have a larger range than the updated models (Figure 6.4). After the first update narrows the spread of flow rate, the following updates change little. Although the spread is still wide, the range is acceptable within the large measurement errors.
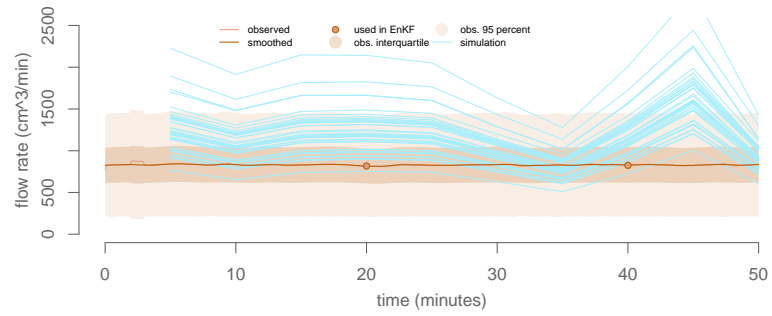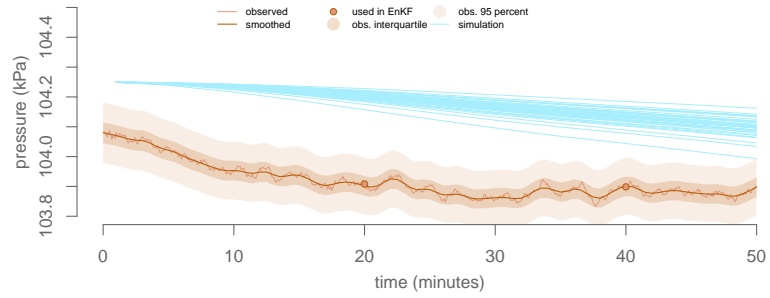
(a) THE INITIAL MODEL RUN
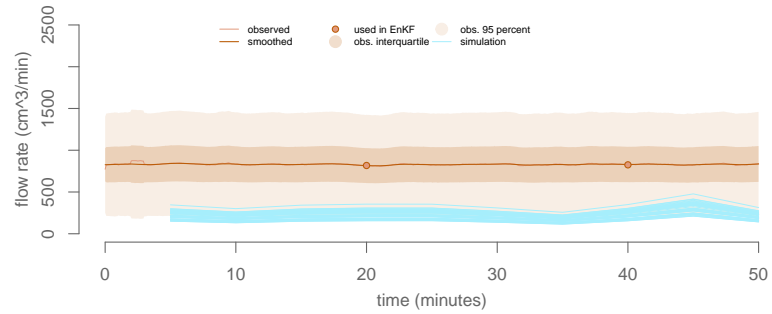
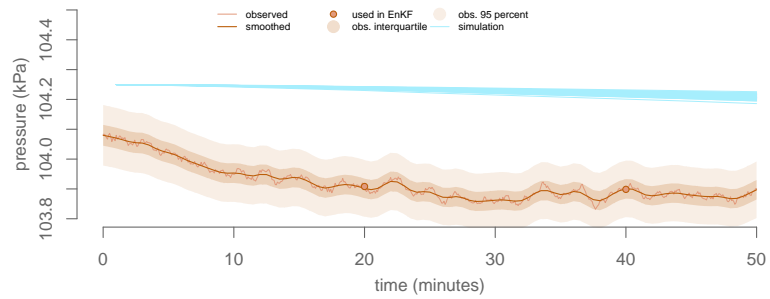(b) CALCULATIONS OF THE UPDATED MODELS AT STEP 2

(c) CALCULATIONS OF THE UPDATED MODELS AT STEP 4

FIGURE 6.4. Flow rate output from the initial and updated models. The flow rate (thin orange line) has been smoothed (thicker orange line; R Core Team, 2012). The 95 percent confidence region (light orange) and interquartile range (medium orange) are shown for the observations. The simulation results of sand tank models (light blue lines) are mostly within the interquartile range of the observations, and always within the 95 percent confidence interval. Two points (shown as orange circles) are used for the history match. Forty simulations were used.
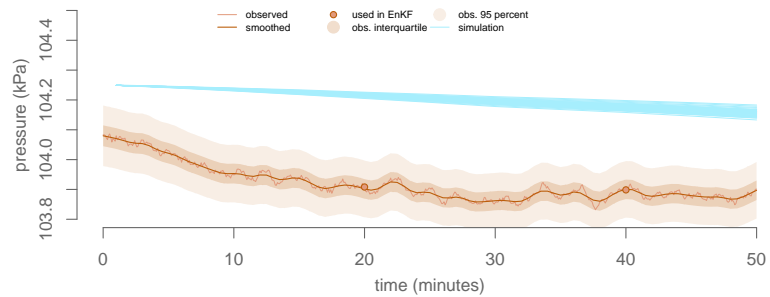
2. The bottom–hole pressure calculated using the initial models has a larger range. Updates improve the simulation results of the sand tank models, and the bottom–hole pressures calculated using the updated models are much

(a) The initial model run

(b) Calculations of the updated models at step 2

(c) Calculations of the updated models at step 4

FIGURE 6.5. Pressure of monitoring well No.1 output using initial and updated models. The pressure (thin orange line) is smoothed (thicker orange line; R Core Team, 2012). The 95 percent confidence region (light orange) and interquartile range (medium orange) are shown for the observations. The simulation results of sand tank models (light blue lines) are converged but deviated from the observations. Two points (shown as orange circles) are used for the history match. Forty simulations were used.

converged and show the same trend (Figure 6.5). However, the pressure data can not be matched, especially for the monitoring wells 1 and 4. One possible cause is the uneven bottom of the sand tank.

One feature appears that the calculated bottom–hole pressure at the monitoring wells using the updated models are always higher than the experiment results and the differences between them are almost constant (Figure 6.6). The differences are probably caused by uneven bottom of the sand tank. So in the following history matching process a makeup will be added to the observation data (Table 6.1).
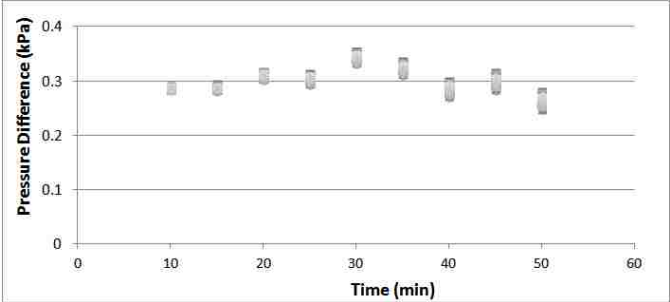
(a) Pressure differences for monitoring well 1
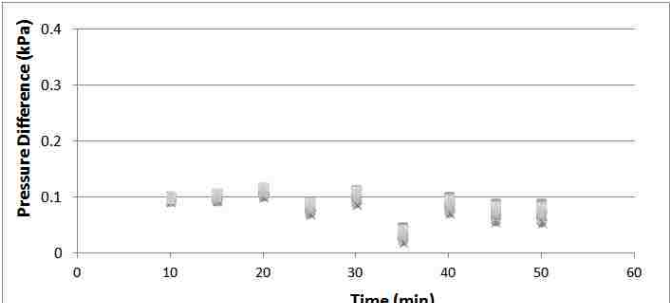
(b) Pressure differences for monitoring well 2
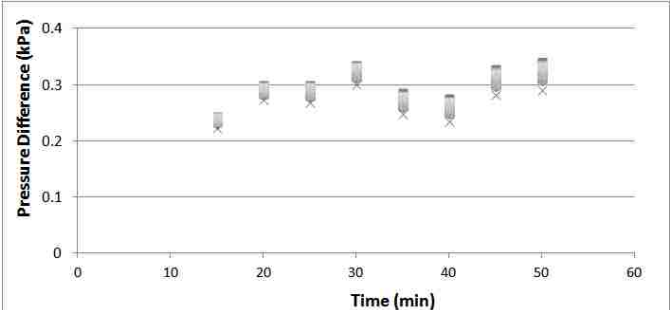
(c) Pressure differences for monitoring well 4

FIGURE 6.6. The bottom–hole pressure differences between simulation results and the observation. The simulation results are calculated using the updated models at step 4. The differences are calculated every five minutes.

TABLE 6.1. A linear regression and statistic analysis were done to the discrepancy between calculated and observed bottom–hole pressures. Here shows the analysis result and it indicates the discrepancies are almost stay constant which probably caused by uneven bottom of the sand tank.

Well ID	Slope	P-value	Average (kPa)	water height (cm)
Monitoring Well 1	-0.000333	0.617	0.299	3.07
Monitoring Well 2	-0.000944	0.118	0.085	0.87
Monitoring Well 4	0.001303	0.180	0.271	2.78

6.3.3 Model Updating with Corrected Observation Data

After the analysis of primary history matching results, a better understanding of the sand tank experiment has been obtained, then we start over the integration of the sand tank experiment data. Here, we correct observed bottom–hole pressures of the monitoring wells and keep updating the near wellbore permeability and porosity (Figure 6.7).

Since the predicted flow rates using the initial models spread over a wild range, the observation data are integrated at 20th, 40th, 60th and 80th minutes. For the flow rate, the spreads of the Ensemble predictions are reduced after each data integration, and almost all the predictions are lower than the measurements, after the data integration at 160th minute, all the predictions of flow rates fall into range of 200 to 500 cm^3/min. Because the flow meter used in the experiment has a large relative error — 38 percent, even though the predictions are much less than the observations (around 830 cm^3/min), they are still acceptable (Chollett, 2012).

For the bottom–hole pressure of the monitoring wells, the predictions are always in an acceptable range. The data integration in the first several steps does not improve the predictions very much (Figure 6.7). Since the predictions are spread and deviated from the measurements at the 160th minute, the observations are integrated and the models were updated. The predictions with updated models are improved and close to the measurements.

(a) HISTORY MATCH TO PRESSURE, WELL 1

(b) HISTORY MATCH TO PRESSURE, WELL 2

(c) HISTORY MATCH TO PRESSURE, WELL 4
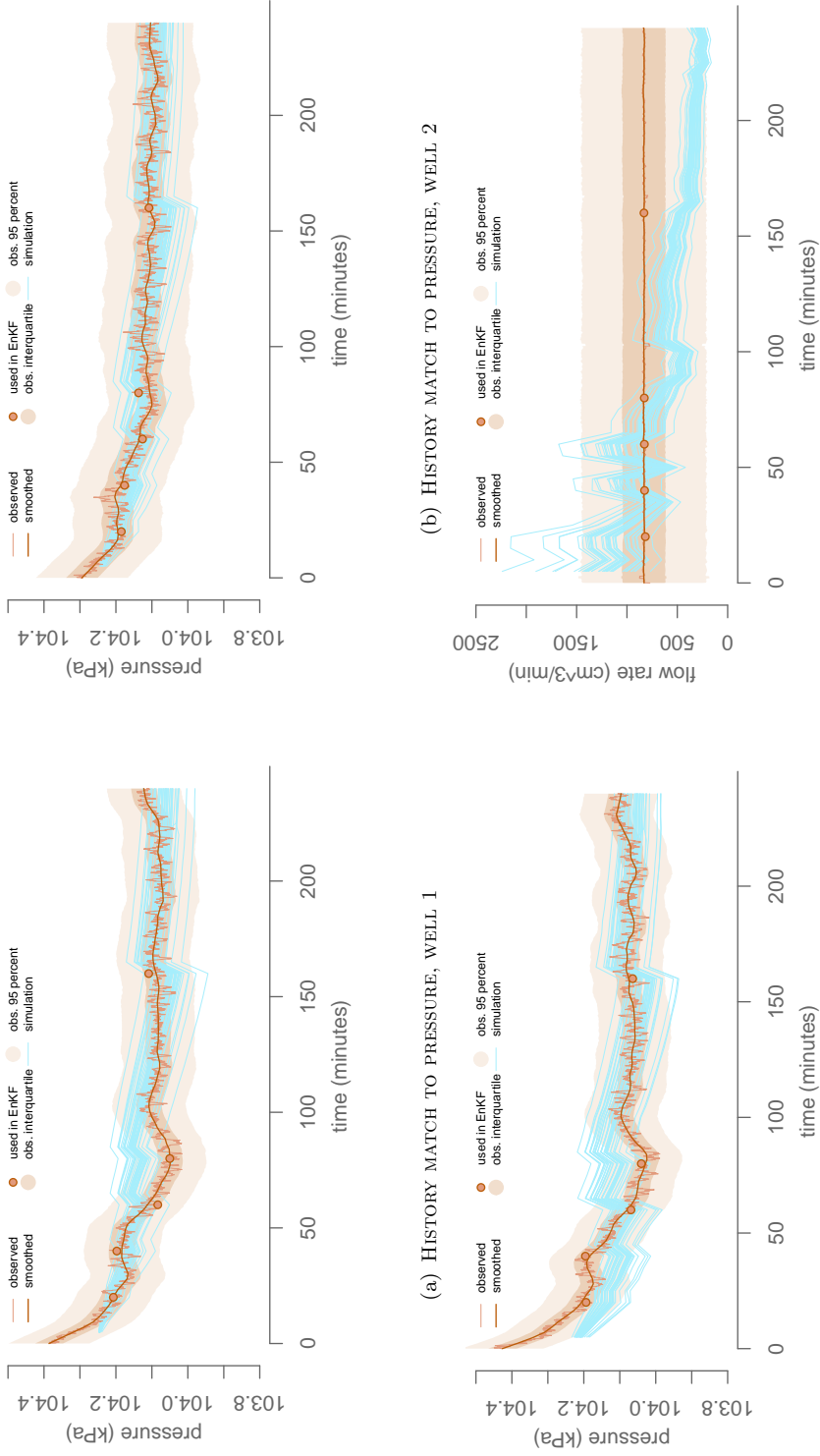
(d) HISTORY MATCH TO FLOW RATE, PRODUCTION WELL

FIGURE 6.7. History matching results for sand tank experiment 2. The pressure or flow rate (thin orange line) has been smoothed using a lowess fit (thicker orange line; R Core Team, 2012). The 95 percent confidence region (light orange) and interquartile range (medium orange) are shown for the observations; the simulations (light blue lines) are mostly within the interquartile range of the observations, and always within the 95 percent confidence interval. Five points (shown as orange circles) are used for the history match. Forty simulations runs; thus, the 95 percent confidence range for the simulations includes all but the single lowest and highest results at any given time. The simulation 95 percent confidence interval has only minor excursions outside the observation interquartile range, and none outside the observation 95 percent confidence interval.

72

The case tests the performance of the EnKF method when some of the observation data has low quality, and the result showed that even if the observation data has a large error (38% measurement errors), the EnKF method still works and brings reasonable results.

6.4   Seismic Data Analysis

The seismic data in the sand tank are collected in both dry and wet conditions, and the seismic first arrival times are picked, because based on the design of this experiment they will be integrated to improve the flow models (Chapter 4). To integrate the first arrival time, both simulated and observed first arrival time are needed and the simulated first arrival time is obtained by running the seismic raytracing on the velocity models.

Since the seismic first arrival times collected at different time are almost the same (Figure 6.8), we can not use them to improve the flow models, but we can still compare the simulated and observed first arrival times. For the dry tank case, the simulated and observed first arrival times match (Figure 6.9) and this proved that the velocity of sand tank can be calculated correctly by Hertz-Mindlin theory and Gassmann equation (Chapter 2). For the wet tank, Figure 6.10 shows that the simulated first arrival time was much earlier than the observed one at the receivers more than 40 cm away from seismic source. It was caused by the calculated high velocity zone near the water table since we assume that the residual air saturation was zero and the tank was fully saturated below the water table. After we chang the residual air saturation to 20%, the simulated and observed first arrival time can be matched (Figure 6.11). The results show that in the first experiment the sand tank was not fully saturated below the water table and the high velocity zone can not be found.
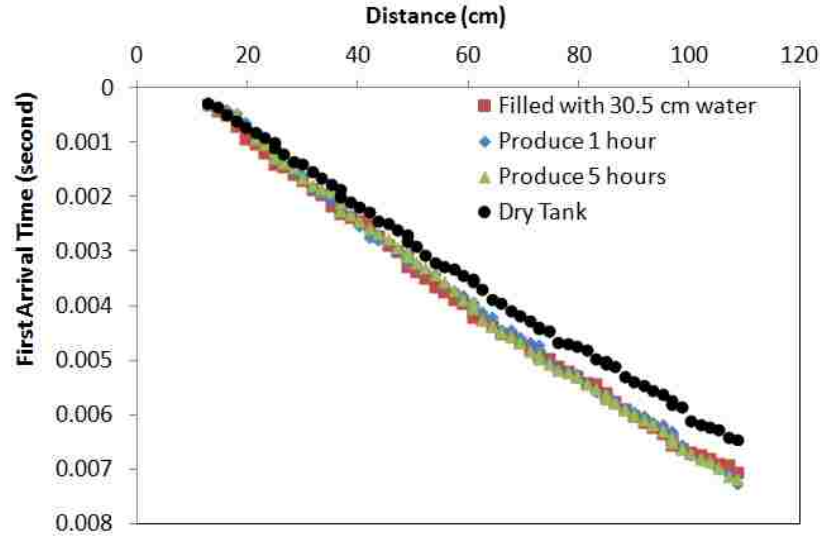
FIGURE 6.8. First arrival times selected from raw seismic data. Seismic source is located at original point. The black circles show the first arrival times for the dry tank case. For the wet tank, the red squares, blue diamonds and green triangles show the first arrival time obtained at initial, 1 hour production and 5 hours production conditions separately. The first arrival times of the dry tank are different from the ones of wet tank, because there was no water in the dry tank and the seismic velocities are different from the ones in the wet tank. The first arrival times of wet tank collected at different time steps are almost the same , because the water pumped out is only a small amount compared to the whole tank, and the water table level only changed a little bit (less than 1 *cm*) during the experiment.

6.5   Conclusions

In this chapter, both the production and seismic data in the first experiment are analyzed and the production data are integrated to improve the sand tank models. For the production data, although the measured flow rates have large errors, EnKF still can reduce the uncertainty of the sand tank models, and the predictions are in the acceptable range, which means EnKF method can handle the observations with large measurement errors. For seismic data, the simulated first arrival time can match the observed ones for the dry tank case. When the sand tank is filled with water, the observed first arrival time can only be matched if we consider the existence of irreducible air which means that the sand is not fully saturated.
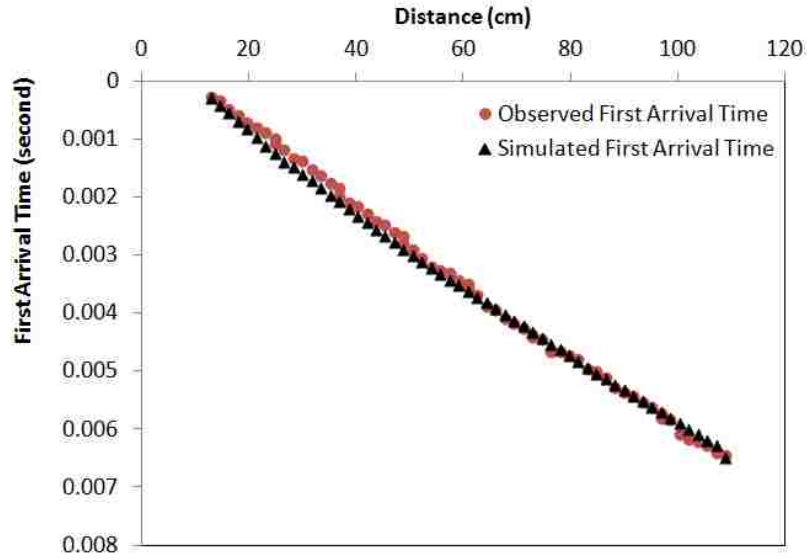
FIGURE 6.9. Simulated seismic first arrival time of the dry tank. The x–axis is the receiver position in centimeter and y–axis is first arrival time in second. The red circles show the observed first arrival time and the black triangles show the simulated first arrival time.
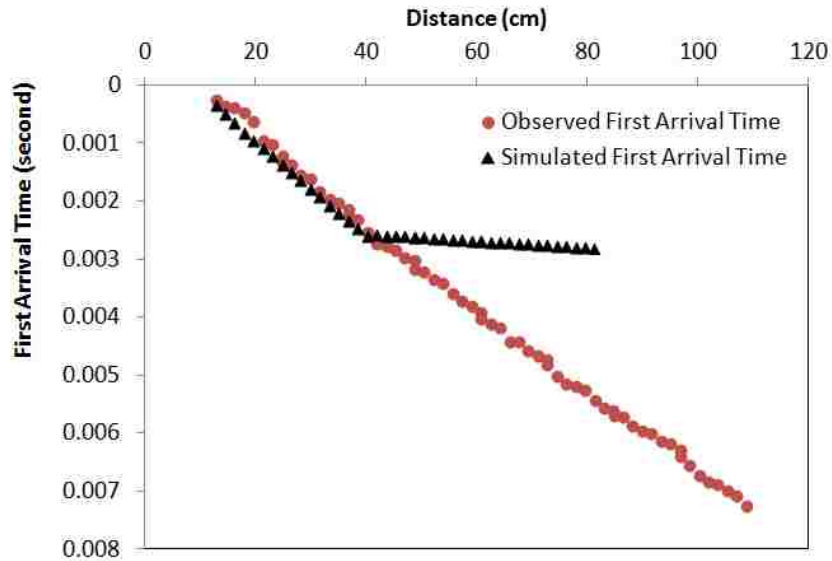
FIGURE 6.10. Simulated seismic first arrival times (triangles) of the wet tank calculated using zero residual air saturation. The red circles show the observed first arrival times and the black triangles show the simulated first arrival time. The simulated first arrival times are matched for the receivers near the source (less than 40 *cm*), but are very different for the receivers far away from the source (more than 40 *cm*).

FIGURE 6.11. Simulated first arrival time of the wet tank calculated using 20% residual air saturation. The red circles show the observed first arrival time and the black triangles show the simulated first arrival time. The simulated and observed first arrival time is matched well.
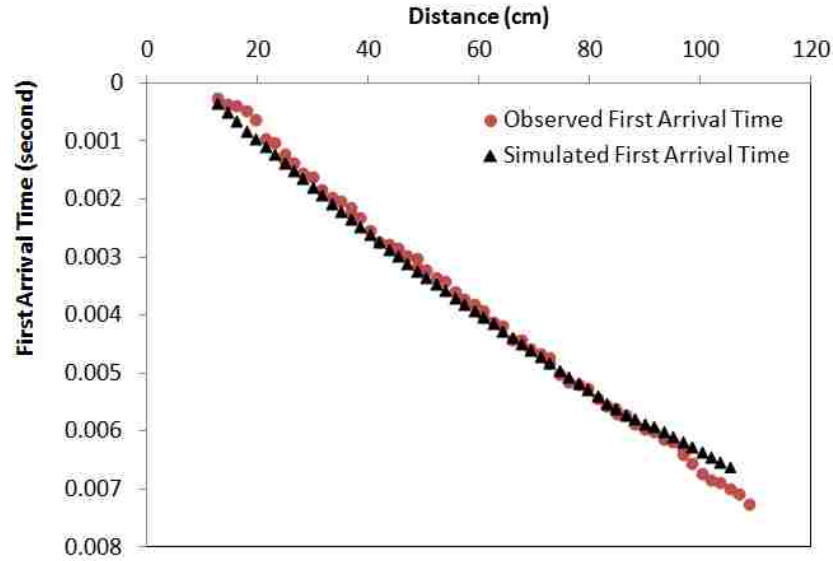
Because the sand below the water–air contact is not fully saturated and the water level change less than 1 cm, first arrival times collected at different time steps are almost the same and can not be used for history matching.

6.6 Recommendations

This chapter describes the first try on the sand tank experiment data integration. The analysis and results provide the several references for the subsequent experiments:

- Since the bottom of the tank is uneven, the water height in each well should be measured, and used for simulation result correction.

- The flow meter does not work well, since its measurement range is too big for the flow rate in the sand tank experiment. So a new flow meter may be needed or we need another way to measure the flow rate.

- The first arrival of seismic data collected at different time steps are almost the same, since the water level changes less than 1 cm from beginning to the end. A new experiment design is needed for testing the integration of seismic first arrivals, and it must be able to provide large water level changes.

Chapter 7
Analysis and Integration of Experimental Data with Small Errors

7.1 Introduction

In Chapter 6, the first sand tank experiment results are discussed and applied to test the EnKF method. Although there are large errors in flow rate, a reasonable result is obtained. Based on the conclusion in Chapter 6, the second sand tank experiment is conducted and the collected data are more reliable. In the second sand tank experiment only production data are collected and integrated to test the performance of the EnKF method. Since the quality of data is good, production history is easy to match.

7.2 Second Sand Tank Experiment

The second experiment is conducted by Ting Sun and Jie Shen. Five water wells are placed at different locations to mimic field production behavior. Production data are collected. The experiment consists of three parts: preparation, sensor calibration and experiment.

7.2.1 Preparation

First, the sand is mixed to provide homogeneous properties (permeability and porosity). The sand tank is shaped with a slope at one side (Figure 2.1) and the wells are placed at five locations (Figure 7.1).

Second, the tank is filled until the water level is 50 cm high and the water is allowed to stand about seven hours so that it can thoroughly permeate sand, and the water levels in all the wells are recorded (Table 7.1). Because the sand tank leaks, after another 8 hours the water level in production well drops to 42.5 cm.

Water level changes in all wells (Table 7.1) are nearly the same; this means the water completely permeated throughout the entire sand tank.
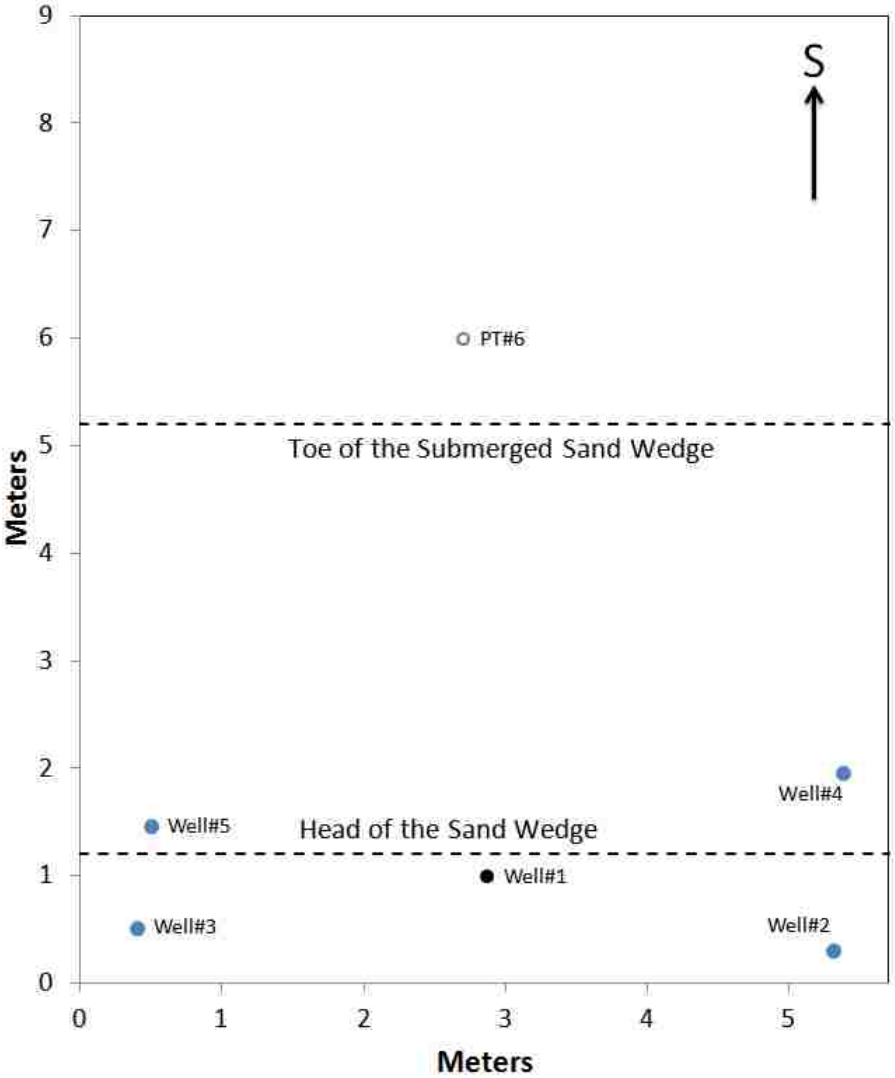
FIGURE 7.1. The locations of the wells in the second experiment. For the second experiment, each well had a pressure and temperature (PT) sensor placed at its bottom and the PT sensor #6 (blue circle without solid fill) is placed at the open water area to record the changes of boundary conditions. Well # 1 (black circle with solid fill) was the production well and all the other wells (blue circles with solid fill) are used as monitoring wells.

TABLE 7.1. Water level records of each well at different times.

Well ID	Head^a at 7 hrs, cm	Head at 15 hours, cm	Head change, cm
Well 1	43.1	42.5	0.6
Well 2	42.1	41.5	0.6
Well 3	43.1	42.5	0.6
Well 4	40.0	39.5	0.5
Well 5	43.6	43.0	0.6

^{a} Datum is base of tank.

7.2.2 Sensor calibration

Data output by the pressure and temperature sensors are in units of voltage, which must be converted to pressure (kPa). The calibration is done by using the sensors to measure different known pressures, and finding out the linear relationship between voltage and pressure. Here is the procedure:

- put all the sensors in a bucket vertically and make sure the end of sensors touched the flat bottom of the bucket;

- fill the bucket with water to 5 different heights, and record data from PT sensors in voltage;

- calculate the pressure at 5 different heights, and compare them with recorded data, then a linear relationship can be found by using the linear least square fit.

  by using linear least square fit find out the linear relationship between voltage data from sensors and the pressure value (Figure 7.2).

7.2.3 Experiment

The experiment uses the following procedure:

- turn on the data collection equipment and the computer, and make sure they all work well;
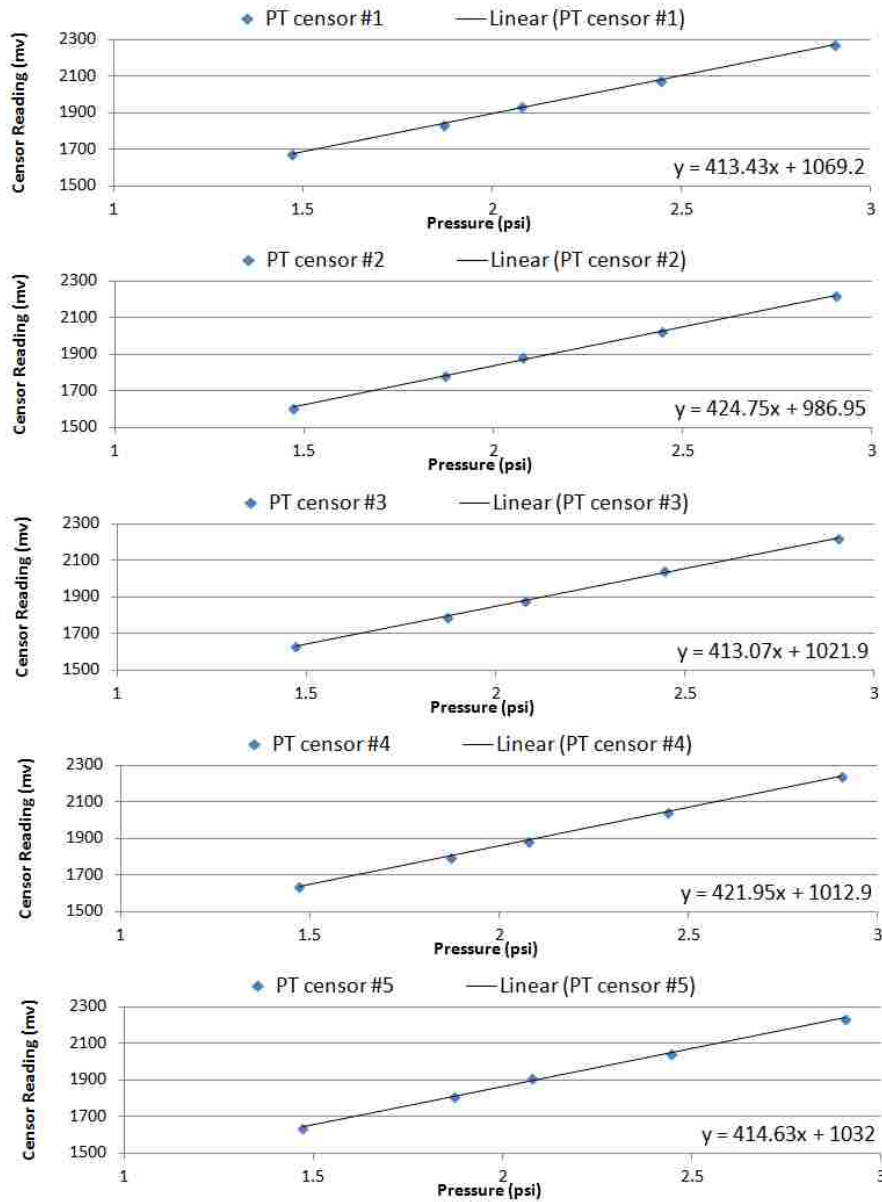
FIGURE 7.2. The calibration formula for PT censors are derived by curve fitting, assuming the linear relation between the output of censors in voltage and the actual pressures.

- turn on the pump and start to pump the water out of the production well;

- measure the flow rate of production well with a graduated cylinder every 5 to 10 minutes.

The experiment lasts for 4 hours. Flow rate data (Figure 7.3) are saved to hard disk and the voltage data from the PT sensors are converted to *psi* units (Figure 7.4).

Although the pump is set up to produce at a constant rate, the measured flow rate increases with time. One possible reason is that when we fill the tank, the water can not displace all the air in the sand and residual air bubbles remain. As the experiment goes on, both water and air are produced and less air is left in the sand, so the air production rate decreases. Because the pump produces constant volume of water and air, while the air production rate decreases, the water production rate (flow rate) increases.
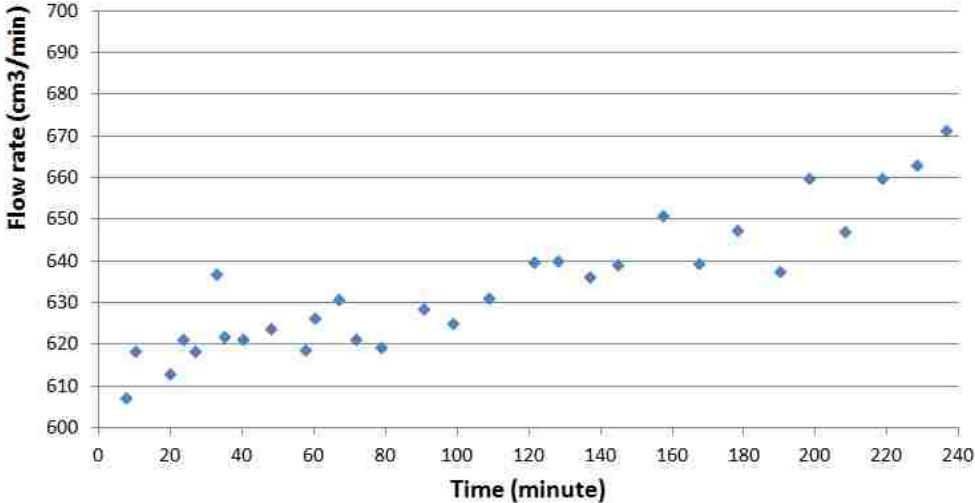

FIGURE 7.3. The flow rate data from the production well. Bubbles stuck in the flow meter make the flow rates measured by flow meter unreliable. Here the flow rate was derived by measuring the amount of produced water in a certain time period (between 80 and 100 seconds) using graduated cylinders, so only limited number measured points are shown. Overall the plot shows that the flow rate increases with time.

7.3   Production Data Integration

To integrate the sand tank experiment data, 40 initial models are generated using the unconditional simulation method, and the reservoir simulation runs with the bottom hole pressures of the production well as the constraint. The bottom hole pressures of the monitoring wells and the flow rate of production well are then integrated at 20 minutes and 37 minutes. The predictions using updated models
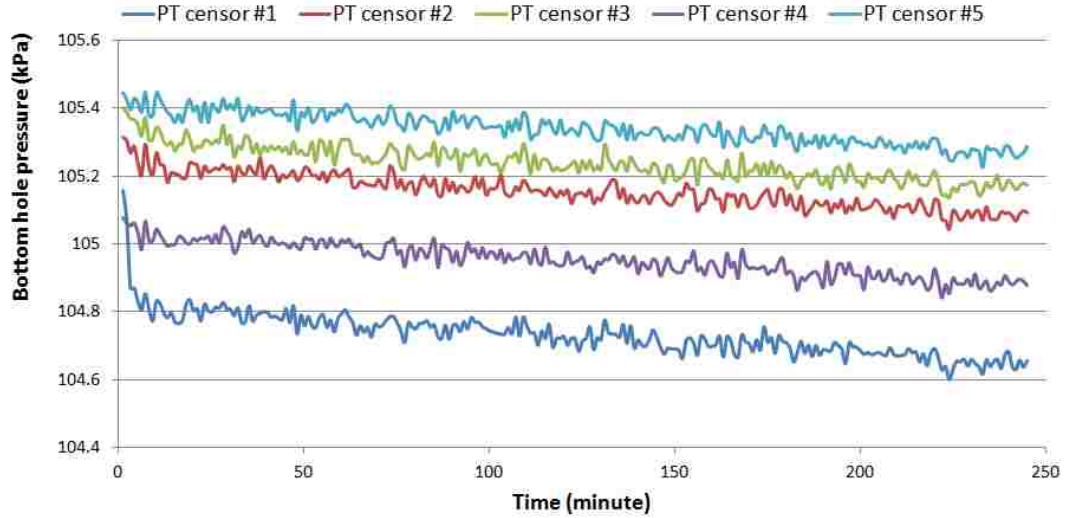
FIGURE 7.4. The blue curve at the bottom shows the pressure measured at the production well, and the others represent the pressures at the monitoring wells. All the bottom hole pressures decrease with time, and have a similar decreasing gradient. The bottom hole pressure of the production well has a jump in the beginning when production started.

have better results (Figuire 7.5 and 7.6) which has less spread and are more close to the observation.

7.4 Summary

In this chapter, the second sand tank experiment has been introduced, including preparation, data collection and calibration. Because the first experiment has provided some references, better data are collected in the second experiment. The data of the second experiment are easy to match and explain since their quality are much better than the first one.

History matching results prove that the EnKF method can be used for the sand tank data integration and its updating results can improve the predictions. Secondly, because the sand tank experiment data is the real data, not synthetic data, the history matching results prove that the EnKF method can be used for real data integration which means that the EnKF method also can be applied to the real reservoir history matching.
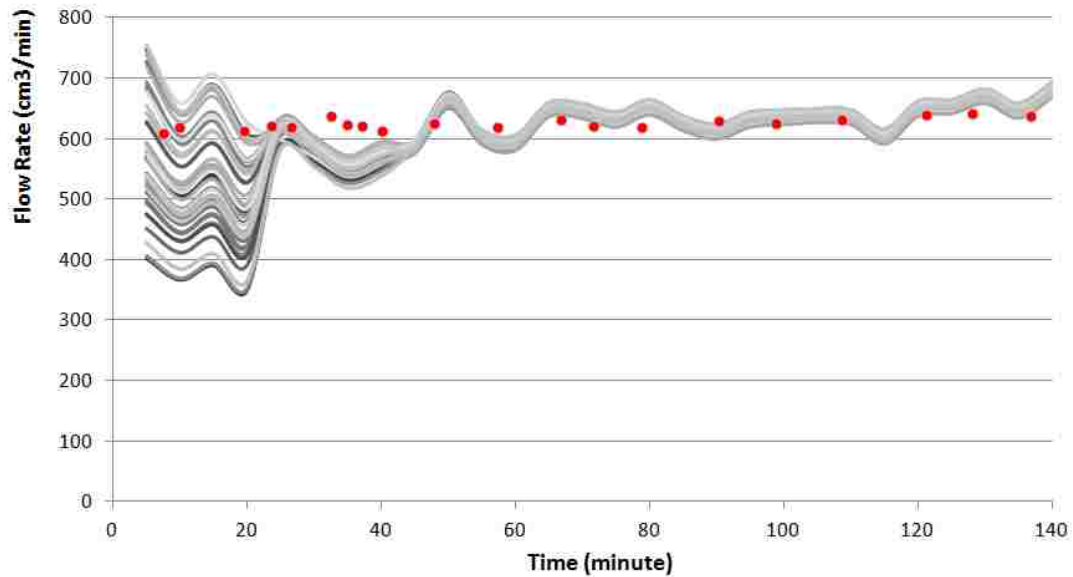
FIGURE 7.5. Evolution of predicted production rates for the second sand tank experiment. The grey curves indicate the simulations of forty models which are generated by using unconditional gaussian simulation and the red points indicate the measured flow rate. The models are updated at 20 minutes and 37 minutes. For the flow rates, the first 20 minutes are predicted with the initial models, and the spread of ensemble is large. With EnKF updating at 20 minutes, the prediction of flow rate are improved and the spread of the ensemble is reduced significantly, and the predictions are "close" to the measurement. At the 37th minute, the observation data are integrated again, and after this step, the spread of the ensemble is reduced, not as much as previous updating step, but the prediction is much closer to the measurements.
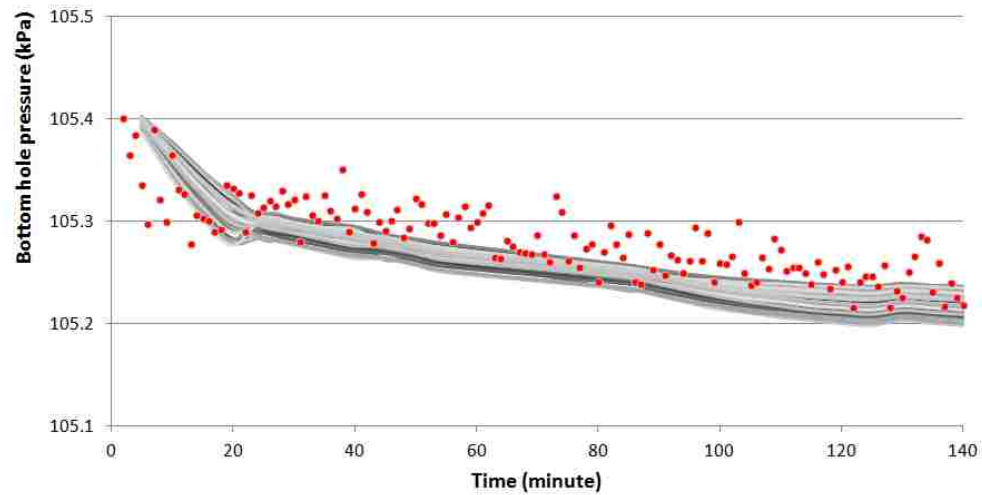
(a) BOTTOM HOLE PRESSURES OF MONITORING WELL 2
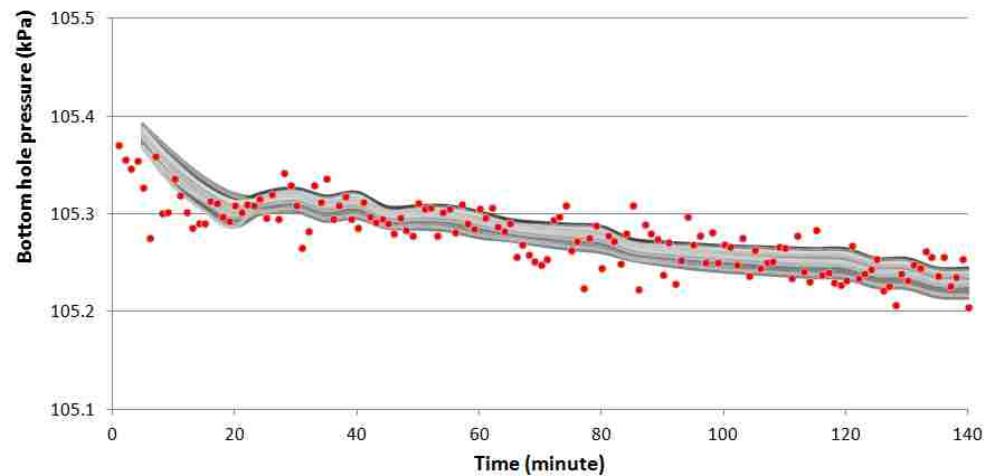
(b) BOTTOM HOLE PRESSURES OF MONITORING WELL 4

FIGURE 7.6. Evolution of predicted bottom hole pressure for the second experiment data. The grey curves are the ensemble of models and the red points are the measured bottom hole pressures. The models are updated at 20 minutes and 37 minutes. For the bottom hole pressures of the monitoring wells, the prediction was close to the measurement result in the beginning, but the uncertainty of the predictions increases with time. After the updating at the 20th and 37th minutes, the spreads of predicted bottom hole pressures are reduced a little bit, since it has been already small.

Chapter 8
Conclusions and Recommendations

8.1 Conclusions

The main objective of this dissertation is to build a continuous reservoir model updating workflow to integrate the sand tank experiment data including both production and seismic data. Because the data are high–frequency sequential data with noise, the EnKF method is used to efficiently integrate them.

Sand tank flow and acoustic properties are needed for the reservoir simulation and seismic raytracing. Because the experiments are run under normal temperature and pressure condition, the property values are easy to be estimated or found in the references. To better understand the problem, scaling analysis and seismic resolvability analysis are done on the capillary transition zone. In the scaling analysis, two new dimensionless numbers are introduced—capillary time and capillary length. We found that for different models, if their capillary number and gravity number are equal, the capillary time would be the same. The scaling analysis results help us find a proper flow rate for the sand tank experiment. In the seismic resolvability analysis, the results indicate that the water table is the main factor affecting first arrival time. The velocity profile above the water table also affects the first arrival time and ray path, but to a lesser degree. Based on the above conclusion, the seismic first arrival time is determined by flow model properties, so it is reasonable to attempt to integrate it to decrease flow model uncertainty.

Two experiments have been done to test the workflow and the EnKF method. In the first one, both the production and seismic data are analyzed and production data are integrated to improve the sand tank simulation models. For the produc-

tion data, there are large errors in the measurements, which makes the data hard to be explained or matched. The analysis and primary match are done before integrating the observations. Based on the primary match results, we have a better understanding of the sand tank experiment, reservoir models and the observations. A better match is obtained after applying the corrections to observations. For the dry sand, the simulated first arrival time can match the observed ones. When the sand tank is filled with water, the observed first arrival time can only be matched if we consider the existence of irreducible air which means that the sand is not fully saturated. Because the sand below the water–air contact is not fully saturated and the water level only changes very little, first arrival times collected at different time steps are almost the same and can not be used for history matching. This case provides the references for the following experiment and tests performance of the EnKF method. The history matching results demonstrate that even if the observation data has large error, the EnKF method still works and brings reasonable results.

In the second experiment, the errors of flow rate are reduced by measuring manually with a graduated cylinder. The level differences of each well location are also measured and used to correct the observed bottom hole pressure of the monitoring wells. Because the data quality are much better in the second experiment, the observations can be matched easily.

8.2   Recommendations

The recommendations are summarized as follows:

- Regarding the experimental setup, currently the flow rate is measured manually, which is an impediment to apply the automatic history matching, so a new way to measure the flow rate automatically is needed.

- Several saturation meters should be added to the experiment to measure the saturations at different depth and locations. The measurements can be used to verify the history matching results or as observation variables to integrate with the sand tank models.

- One of the advantages of the sand tank experiment is that we can design the experiment based on the need. The sand tank experiments applied in this dissertation are simple, since only one production well is placed. For future work, we can change the shape of the sand tank, add production and injection wells, or place an artificial "fault" (a piece of wood).

- The capillary pressure and permeability data used are obtained from the reference (Lauer and Engel, 2005). To make the simulation results more reliable, we can measure the true capillary pressure and relative permeability to incorporate them into the reservoir simulation.

- The seismic first arrival times are mainly determined by water table levels, so if we would like to integrate seismic first arrival times, there should be a dynamic monitoring of the water table change during the experiment.

References

[1] Aanonsen, Sigurd. (2008). Efficient History Matching Using a Multiscale Technique. SPE Reservoir Evaluation & Engineering, pp. 154-164.

[2] Ahmed, Tarek. (2010). Reservoir Engineering Handbook. 4th. Gulf Professional Pub.

[3] Ahner, P.F., and A.H. Su. (1994). Physical Model Steamood Studies Using Horizontal Wells. SPE Reservoir Engineering 9 (1): 59 - 66.

[4] Alpak, Faruk O., Florian van Kats, and Detlef Hohl. (2009). Stochastic History Matching of a Deepwater Turbidite Reservoir. SPE Reservoir Simulation Symposium. The Woodlands, Texas. SPE-119030-MS.

[5] Amyx, James W., Daniel M. Bass, and Robert L. Whiting. (1960). Petroleum Reservoir Engineering - Physical Properties. McGraw-Hill Book Company, Inc.

[6] Anderson, Je?rey L. (2001). An Ensemble Adjustment Kalman Filter for Data Assimilation. Monthly Weather Review, vol. 129.

[7] Bachrach, Ran, Jack Dvorkin, and Amos Nur. (1998a). High-resolution shallow- seismic experiments in sand, Part II: Velocities in shallow unconsolidated sand. Geophysics 63 (4): 1234-1240 (July-August).

[8] Bachrach, Ran, Jack Dvorkin, and Amos Nur. (1998b). High-resolution shallow-seismic experiments in sand, Part I: Water table, uid ow and saturation. Geophysics 63 (4): 1225-1233 (July-August).

[9] Bachrach, Ran, Jack Dvorkin, and Amos Nur. (2000). Seismic velocities and Poissons ratio of shallow unconsolidated sands. Geophysics 65 (2): 559-564.

[10] Beard, D.C., and P.K. Weyl. (1973). Inuence of Texture on Porosity and Permeability of Unconsolidated Sand. The American Association of Petroleum Geologists Bulletin 57 (2): 349-369 (February).

[11] Biot, M.A. (1956a). Theory of Propagation of Elastic Waves in Fluid-Saturated Porous Solid. I. Higher-Frequency Range. The Journal of the Acoustical Society of America 28(2) (March): 179-191.

[12] Biot, M.A. (1956b). Theory of Propagation of Elastic Waves in Fluid Saturated Porous Solid. II. Low-Frequency Range. The Journal of the Acoustical Society of America 28(2) (March): 168-178.

[13] Buckingham, E. (1914). On Physically Similar Systems: Illustrations of The Use of Dimensional Equations. Phys. Rev. 4 (4): 345-376.

[14] Center for Wave Phenomena. (2012). Seismic Unix project. software download and documentation site.

[15] Chen, Y., Dean S. Oliver, and Dongxiao Zhang. (2009). Data Assimilation for Nonlinear Problems by Ensemble Kalman Filter with Reparameterization. Journal of Petroleum Science and Engineering 66(1-2) (May): 1-14.

[16] Chen, Yan. (2008). Ensemble-Based Closed-loop Production Optimization. Ph.D. diss., University of Oklahoma.

[17] Chollett, Shannon. (2012). An Experimental and Theoretical Critique of Flow Model Accuracy. Masters thesis, Louisiana State University.

[18] CMG. (2009). IMEX Users Guide - Version 2009.

[19] Collins, Royal Eugene. (1976). Flow of Fluids through Porous Materials. Litton Educational Publishing, Inc.

[20] Craig, Jr., Forrest F. (1975). The Reservoir Engineering Aspects of Waterooding. Volume 3 of SPE Monograph Series. Dallas, Texas: Society of Petroleum Engineers.

[21] Deutsch, Clayton V., and Andre G. Journel. (1994). The Application of Simulated Annealing to Stochastic Reservoir Modeling. SPE Advanced Technology Series 2(2):222 - 227. 23565-PA.

[22] Dong, Yannong. (2005). Integration of Time-Lapse Seismic Data into Automatic History Matching. Ph.D. diss., The University of Oklahoma.

[23] Dullien, F. A. L. (1979). Porous media: Fluid transport and pore structure. Academic Press.

[24] Echevin, Vincent, Pierre De Mey, and Geir Evensen. (2000). Horizontal and Vertial Structure of the Representer Functions for Sea Surface Measurements in a Coastal Circulation Model. Journal of Physical Oceanography 30 (10): 2627-2635.

[25] Eigestad, Geir Terje, and Johne Alex Larsen. (2000). Numerical Modelling of Capillary Transition Zones. SPE Asia Pacic Oil and Gas Conference and Exhibition. Brisbane, Australia. SPE-64374-MS.

[26] Emerick, Alexandre Anoze, Rafael Jesus de Moraes, and Jose Roberto Pereira Rodrigues. (2007). History Matching 4D Seismic Data With E?cient Gradient-Based Methods. EUROPEC/EAGE Conference and Exhibition. London, U.K. SPE-107179-MS.

[27] Engle, J., T. Schanz, and C. Lauer. (2005). State parameters for unsaturated soils, basic empirical concepts. Springer Proceedings in Physics 94 (1): 125-138.

[28] Evensen, G. (1994). Sequential Data Assimilation With a Nonlinear Quasi-Geostrophic Model Using Monte Carlo Methods to Forecast Error Statistics. J. Geophys. Res. 99 (C5): 10143-10162.

[29] Evensen, G. (2004). Sampling Strategies and Square Root Analysis Schemes for the EnKF. Ocean Dynamics 54:539-560.

[30] Everdingen, A.F. Van, and W. Hurst. (1949). The Application of the Laplace Transformation to Flow Problems in Reservoirs. Petroleum Transactions, AIME 186 (December): 305-324.

[31] Gao, Guohua, and Albert C. Reynolds. (2006). An Improved Implementation of the LBFGS Algorithm for Automatic History Matching. SPE Journal 11(1) (March): 5-17. SPE-90058-PA.

[32] Gassmann, Fritz. (1951). Elastic Waves through a Packing of Spheres. Geophysics 16(4) (May): 673-685.

[33] Genuchten, M.TH. Van. (1980). A Closed-form Equation for Predicting the Hydraulic Conductivity of Unsaturated Soils. Soil Science Society of America Journal 44(5):892-898.

[34] Ghamdi, Bander N. Al, and Luis F. Ayala. (2010). Analysis of Capillary Pressure and Relative Permeability E?ects on the Productivity of Naturally Fractured Gas-Condensate Reservoirs. SPE/DGS Saudi Arabia Section Technical Symposium and Exhibition.

[35] Goovaerts, Pierre. (1997). Geostatistics for Natural Resources Evaluation. New York City: Oxford.

[36] Gosselin, O., S.I. Aanonsen, I. Aavatsmark, A. Cominelli, R. Gonard, M. Kolasinski, F. Ferdinandi, L. Kovacic, and K. Neylon. (2003). History Matching Using Time-lapse Seismic (HUTS). SPE Annual Technical Conference and Exhibition. Denver, Colorado. SPE-84464-MS.

[37] Gu, Yaqing, and Dean S. Oliver. (2005). History Matching of the PUNQ-S3 Reservoir Model Using the Ensemble Kalman Filter. SPE Journal 10 (June): 217-224. SPE-89942-PA.

[38] Gunning, James, and Michael E Glinsky. (2004). Delivery: an open-source model-based Bayesian seismic inversion program. Computers & Geosciences 30(6):619-636.

[39] Hawkins, Murry F. (1956). A Note on Sjub E?ect. Petroleum Transactions, AIME 207 (July): 356-357.

[40] Horne, Roland N. (1995). Modern Wel l Test Analysis. Second. Petroway.

[41] Houtekamer, P. L., and H. L. Mitchell. (2001). A Sequential Ensemble Kalman Filter for Atmospheric Data Assimilation. Mon. Weather Rev. 129(1) (3): 123-137.

[42] Kalla, S., C. D. White, J. Gunning, and M. E. Glinsky. (2009). Downscaling Multiple Seismic Inversion Constraints to Fine-Scale Flow Models. SPE Journal 14 (4): 746-758.

[43] Kalla, Subhash, Christopher D. White, James Gunning, and Michael E. Glinsky. (2008). Consistent Downscaling of Seismic Inversion Thicknesses to Cornerpoint Flow Models. SPE Journal 13(4):412-422.

[44] Krumbein, W.C., and Esther Aberdeen. (1937). The Sediments of Barataria Bay. Journal of Sedimentary Research 7 (1): 3-17 (April).

[45] Larsen, Jone Alex, Trond Thorsen, and Geir Haaskjold. (2000). Capillary Tran- sition Zones from a Core Analysis Perspective. SCA 2000-20. Abu Dhabi, UAE.

[46] Lauer, C., and J. Engel. (2005). A triaxial device for unsaturated sand - New Development. Unsaturated Soil: Experimental Studies 93 (4): 301-314.

[47] Leverett, M.C. (1941). Capillary Behavior in Porous Solids. Petroleum Transactions, AIME 142:152-169.

[48] Li, Gaoming, Mei Han, R. Banerjee, and A.C. Reynolds. (2009). Integration of Well Test Pressure Data Into Heterogeneous Geological Reservoir Models. SPE Annual Technical Conference and Exhibition. New Orleans, Louisiana. SPE-124055-MS.

[49] Li, H., S. Chen, and D. Yang. (2008). Real-Time Reservoir Geological Model Updating Using the Hybrid EnKF and Geostatistical Technique. Canadian International Petroleum Conference. Calgary, Alberta. 2008-128-EA.

[50] Li, Ruijian, A.C. Reynolds, and D.S. Oliver. (2003). History Matching of Three- Phase Flow Production Data. SPE Journal 8(4) (December): 328-340. SPE-87336-PA.

[51] Li, Xin. (2008). Continuous Reservoir Model Updating by Ensemble Kalman Filter on Grid Computing Architectures. Ph.D. diss., Louisiana State University.

[52] Lorentzen, R., K. K. Fjelde, J. Froyen, and G. Nvdal. (2001). Underbalanced and Low-Head Drilling Operation: Real Time Interpretation of Measured Data and Operational Support. SPE Annual Technical Conference and Exhibition. Denver,CO. SPE 71384.

[53] Lorenzo, Juan M., David E. Smolkin, Christopher D. White, Shannon Chollett, and Ting Sun. (2013). Benchmark hydrogeophysical data from a physical seismic model. Computers & Geosciences 50 (Jan): 44-51.

[54] Madsen, H., and R. Canizares. (1999). Comparison of Extended and Ensemble Kalman Filter for Data Assimilation in Coastal Area Modeling. International Journal for Numerical Methods in Fluid 31:961-981.

[55] Mavko, Gary, Tapan Mukerji, and Jack Dvorkin. (1998). The Rock Physics Hand- book: Tools for Seismic Analysis in Porous Media. Cambridge, New York, Melbourne: Cambridge University Press.

[56] Mian, M. A. (1992). Petroleum Engineering Handbook for the Practicaing Engineer. Volume 2. Pennwell Books.

[57] Mualem, Yechezkel. (1976). A New Model for Predicting the Hydraulic Conductivity of Unsaturated Porous Media. Water Resources Research 12 (3): 513-522.

[58] Nvdal, G., T. Mannseth, and E.H. Vefring. (2002). Near-Well Reservoir Monitoring through Ensemble Kalman Filter. 2002 SPE/DOE Improved Oil Recovery Symposium. Tulsa, Oklahoma. SPE-75235.

[59] Oliver, D. S., A.C. Reynolds, and N. Liu. (2008). Inverse Theory For Petroleum Reservoir Characterization and History Matching. Cambridge, UK: Cambridge University Press.

[60] Oreskes, Naomi, Kristin Shrader-Frechette, and Kenneth Belitz. (1994). Verication, Validation, and Conrmation of Numerical Models in the Earth Sciences. Science 263 (5147): 641-646 (February).

[61] Ouenes, A., B. Brefort, G. Meunier, and S. Dupere. (1993). A New Algorithm for Automatic History Matching: Application of Simulated Annealing Method (SAM) to Reservoir Inverse Modeling. Unsolicited. SPE-26297-MS.

[62] Panda, Manmath N., and Larry W. Lake. (1994). Estimation of Single-Phase Permeability from Parameters of Particle-Size Distribution. AAPG Bulletin 78(7) (July): 1028-1039.

[63] Peaceman, D.W. (1983). Interpretation of Well-Block Pressures in Numerical Reservoir Simulation with Non-Square Grid Blocks and Anisotropic Permeability. Society of Petroleum Engineers Journal, June, 531-543.

[64] Pyrcz, M. J. (2004). The Integration of Geologic Information into Geostatistical Models. Ph.D. diss., University of Alberta, Edmonton, Alberta, Canada.

[65] R Core Team. (2012). R: A Language and Environment for Statistical Computing. Vienna, Austria: R Foundation for Statistical Computing.

[66] Reynolds, A.C., R. Li, and D.S. Oliver. (2004). Simultaneous Estimation of Absolute and Relative Permeability by Automatic History Matching of Three Phase Flow Production Data. JCPT.

[67] Reynolds, A.C., M. Zafari, and G. Li. (2006). Iterative Forms of the Ensemble Kalman Filter. European Conference on the Mathematics of Oil Recovery. Amsterdam, Netherlands. A030.

[68] Ruark, Arthur Edward. (1935). Inspectional Analysis: A Method Which Supplements Dimensional Analysis. Journal of Elisha Mitchel l Scientic Society 51:127-133.

[69] Saltzer, Rebecca, and Chris Finn. (2006). Exploiting the non-uniqueness of seismic inversion to obtain alternate scenarios of economic interest. SEG/New Orleans Annual Meeting.

[70] Sambridge, Malcolm. (1999). Geophysical inversion with a Neighbourhood Algorithm: I. Searching a parameter space. Geophys. J. Int. 138:479-494.

[71] Schulze-Riegert, Ralf, Markus Krosche, Oliver Pajonk, and Hassan Mustafa. (2009). Data Assimilation Coupled to Evolutionary Algorithms - A Case Example in History Matching. SPE/EAGE Reservoir Characterization and Simulation Conference. Abu Dhabi, UAE. SPE-125512-MS.

[72] Sen, Mrinal K., Akhil Datta-Gupta, P.L. Sto?a, L.W. Lake, and G.A. Pope. (1995). Stochastic Reservoir Modeling Using Simulated Annealing and Genetic Algorithms. SPE Formation Evaluation 10(1):49-56. SPE-24754-PA.

[73] Shams, M., A.H. El-Banbi, and M. Khairy. (2013). E?ects of Capillary Pressure on the Numerical Simulation of Conventional and Naturally Fractured Reservoirs. North Africa Technical Conference and Exhibition.

[74] Shook, Mike, Dachang Li, and Larry W. Lake. (1992). Scaling Immiscible ow Through Permeabile Media by Inspectional Analysis. In Situ 16 (4): 311-349 (Jan).

[75] Skjervheim, J.-A., G. Evensen, , S.I. Aanonsen, B.O. Ruud, and T.A. Johansen. (2007). Incorporating 4D Seismic Data in Reservoir Simulation Models Using Ensemble Kalman Filter. SPE Journal 12(3):282-292. SPE-95789-PA.

[76] Smolkin, David Elliot. (2011). Laboratory Scale Seismic Analysis of a Spatially Variable Hydrological Surface in Unconned, Unconsolodated Sand. Master. diss., Louisiana State University.

[77] Sprunt, Eve S., Ron E. Gilliland, and Mary L. Barrett. (1993). Predicting the Permeability of Unconsolidated Sediments From Grain Size Measurements. Gulf Coast Association of Geological Societies Transactions 43:373-380.

[78] Strebelle, Sebastien. (2002). Conditional Simulation of Complex Geological Structures Using Multiple-Point Statistics. Mathematical Geology 34(1):1-21.

[79] Swanson, B.F. (1981). A Simple Correlation Between Permeability and Mercury Capillary Pressures. Journal of Petroleum Technology 33 (12): 2498-2504 (December).

[80] Tanaka, Shusei, Norio Arihara, and Muhammad Al-Marhourn. (2010). E?ects of Oil Compressibility on Production Performance of Fractured Reservoirs Evaluated by Streamline Dual-Porosity Simulation. SEP EUROPEC/EAGE Annual Conference and Exhinition.

[81] Tarantola, Albert. (1997). Inverse Problem Theory:Methods for Data Fitting and Model Parameters Estimation. Amesterdam,Netherland: Elsevier.

[82] Tavassoli, Z., Jonathan N. Carter, and Peter R. King. (2004). Errors in History Matching. SPE Journal 9 (3): 352-361 (September).

[83] Tezpur. (2013). Tezpur User Guide. LSU HPC Group.

[84] Thulin, Kristian, Gaoming Li, SigurdIvar Aanonsen, and Albert C. Reynolds. (2007). Estimation of Initial Fluid Contacts by Assimilation of Production Data With EnKF. SPE Annual Technical Conference and Exhibition. Anaheim, California. SPE-109975-MS.

[85] Valestrand, Randi, Jan Sagen, Geir Nvdal, and Olaf Huseby. (2010). The E?ect of Including Tracer Data in the Ensemble-Kalman-Filter Approach. SPE Journal 15(2):454-470. SPE-113440-PA.

[86] Vinsome, P.K.W., and J. Westerveld. (1980). Comparison of A Three-dimensional Numerical Simulation with A ltot Water Drive Physical Model. Journal of Canadian Petroleum Technology 19 (4): 42-45.

[87] Wang, Zhijing. (2001). Fundamentals of seismic rock physics. Geophysics 66 (2): 398-412.

[88] Watanabe, Shingo, Akhil Datta-Gupta, Yalchin Efendiev, and Deepak Deveg- owda. (2009). A Hybrid Ensemble Kalman Filter With Coarse Scale Constraint for Nonlinear Dynamics. SPE Annual Technical Conference and Exhibition. New Orleans, Louisiana. SPE-124826-MS.

[89] Welge, Henry J. (1952). A Simplied Method for Computing Oil Recovery by Gas or Water Drive. Petroleum Transactions, AIME 195:91-98.

[90] Wen, Xian-Huan, and Wen H. Chen. (2007). Some Practical Issues on Real-Time Reservoir Model Updating Using Ensemble Kalman Filter. SPE Journal 12(2):156-166. SPE-111571-PA.

[91] White, Christopher D. (2010). Statistical Reservoir Modeling. PETE7285.

[92] Yilmaz, Oz. (2001). Seismic Data Anyalysis: Processing, Inversion, Interpreation of Seismic Data. Volume II. Tulsa, USA: Society of Exploration Geophysicists.

[93] Zelt, Colin. (1988). FAST 3-D First Arrival Seismic Tomography programs. Download site for RAYINV ray tracing program.

[94] Zhang, F., and A.C. Reynolds. (2002). Optimization Algorithms for Automatic History Matching of Production Data. European Conference on the Mathematics of Oil Recovery.

[95] Zhang, Fengjun, Jan Arild Skjervheim, A.C. Reynolds, and D.S. Oliver. (2005). Automatic History Matching in a Bayesian Framework, Example Applications. SPE Reservoir Evaluation & Engineering 8(3):214-223. SPE-84461- PA.

[96] Zhao, Yong, Albert C. Reynolds, and Gaoming Li. (2008). Generating Facies Maps by Assimilating Production Data and Seismic Data With the Ensemble Kalman Filter. SPE/DOE Symposium on Improved Oil Recovery. Tulsa, Oklahoma. SPE-113990-MS.

Appendix: Capillary Pressure and Parameters for Velocity Calculation

TABLE A.1. Capillary pressure saturation table of Hostun sand (Engle, Schanz, and Lauer 2005). The grain size is similar to the sand tank, and these data are used for sand tank calculations.

Saturation	Capillary Pressure (psi)	Capillary Pressure (kPa)
0.06	1.45	10.00
0.07	1.16	8.00
0.08	0.87	6.00
0.09	0.58	4.00
0.10	0.44	3.03
0.39	0.29	2.00
0.64	0.22	1.52
0.97	0.15	1.03
0.98	0.07	0.48
1.00	0	0

TABLE A.2. The values of the other parameters used to calculate velocities

Quantity	Symbol	Value	Units
Bulk modulus of water	K_{water}	2.2×10^9	Pa
Bulk modulus of air	K_{air}	1.01×10^5	Pa
Mineral bulk modulus	K_0	36.6×10^9	Pa
Framework dry shear modulus	G_{dry}	45.0×10^9	Pa
Water density	ρ_{water}	1000	kg/m^3
Air density	ρ_{air}	0.18	kg/m^3
Mineral density	ρ_{quartz}	2650	kg/m^3

Vita

Ting Sun was born in 1981, in Jinzhou, Liaoning Province, China. He finished his undergraduate studies in China University of Petroleum (Dongying) in July 2005. He earned his master degree from China University of Petroleum (Beijing) as a reservoir engineering student in July 2008. He is currently a candidate for the degree of Doctor of Philosophy in Petroleum Engineering at Louisiana State University, which is expected to be awarded in May 2014.